JGR Oceans

RESEARCH ARTICLE
10.1029/2020JC016861

Rates and Mechanisms of Turbulent Mixing in a Coastal Embayment of the West Antarctic Peninsula

Ryan M. Scott[1,2], J. Alexander Brearley[1], Alberto C. Naveira Garabato[2], Hugh J. Venables[1], and Michael P. Meredith[1]

[1]British Antarctic Survey, Cambridge, UK, [2]Ocean and Earth Science, University of Southampton, National Oceanography Centre Southampton, Southampton, UK

Key Points:

- Underwater glider time series reveals spatiotemporally varying turbulent dissipation and heat flux in Ryder Bay
- Basin-wide thermocline dissipation is associated with near-inertial shear that occurs ~1.7 days after strong wind events
- Elevated dissipation at depth is generally confined to a topographic ridge and is likely controlled hydraulically

Supporting Information:

Supporting Information may be found in the online version of this article.

Correspondence to:

R. M. Scott,
ryacot85@bas.ac.uk

Citation:

Scott, R. M., Brearley, J. A., Naveira Garabato, A. C., Venables, H. J., & Meredith, M. P. (2021). Rates and mechanisms of turbulent mixing in a coastal embayment of the West Antarctic Peninsula. *Journal of Geophysical Research: Oceans*, *126*, e2020JC016861. https://doi.org/10.1029/2020JC016861

Received 7 OCT 2020
Accepted 8 MAR 2021

Abstract Quantifying and understanding the processes driving turbulent mixing around Antarctica are key to closing the Southern Ocean's heat budget, an essential component of the global climate system. In 2016, a glider deployed in Ryder Bay, West Antarctic Peninsula, collected hydrographic and microstructure data, obtaining some of the first direct measurements of turbulent kinetic energy dissipation off West Antarctica. Elevated dissipation $O(10^{-8})$ W kg^{-1} is found above a topographic ridge separating the 520-m-deep bay, where values are $O(10^{-10})$ W kg^{-1}, from a deep fjord of the continental shelf, suggesting the ridge is important in driving upward mixing of warm Circumpolar Deep Water. The 12 glider transects reveal significant temporal variability in hydrographic and dissipation conditions. Mooring-based current and nearby meteorological data are used to attribute thermocline shoaling (deepening) to Ekman upwelling (downwelling) at Ryder Bay's southern boundary, driven by ~3-day-long south-westward (north-westward) wind events. Anticyclonic winds generated near-inertial shear in the bay's upper layers, causing elevated bay-wide shear and dissipation ~1.7 days later. High dissipation over the ridge appears to be controlled hydraulically, being co-located (and moving) with steeply sloping isopycnals. These are observed in ~60% of the transects, with a corresponding mean upward heat flux of ~2.4 W m^{-2}. The ridge, therefore, provides sustained heat to the base of the thermocline, which can be released into overlying waters during the bay-wide, thermocline-focused dissipation events (mean heat flux of ~1.3 W m^{-2}). This highlights the role of ridges, which are widespread across the West Antarctic Peninsula, in the regional heat budget.

Plain Language Summary Glacial ice flowing off the Antarctic continent either terminates directly into the ocean or forms floating tongues called ice shelves. Marine-terminating glaciers and ice shelves in West Antarctica are melting rapidly, contributing significantly to global sea-level rise. The melting has largely been attributed to the presence of warm deep waters, which travel at depth from the shelf break toward the coast, before mixing upwards and coming into contact with ice. However, we lack an understanding of the vertical mixing processes. In 2016, an autonomous underwater robot was used to measure the vertical mixing in Ryder Bay, off the West Antarctic Peninsula. Increased vertical mixing was consistently observed above a ridge on the seafloor at the bay's entrance, suggesting that the ridge is a hotspot for bringing sustained deep-ocean heat to shallower depths. The heat rises until it reaches a strong temperature gradient in the ocean, with colder, less-dense water above. This gradient typically prevents rapid mixing; however, strong winds are found to cause bay-wide intense mixing events that release heat across the gradient into overlying waters. Similar ridges are widespread off the West Antarctic Peninsula, suggesting that they are important regionally for bringing heat toward glaciers and ice shelves.

1. Introduction

Ice shelves in the West Antarctic sector are experiencing the greatest mass loss anywhere in Antarctica, with basal melt rates of up to ~5 m yr^{-1} (Rignot et al., 2013). The melting and thinning of these floating tongues of land-based ice cause the grounded glaciers that feed them to accelerate, contributing significantly to sea level rise (Dupont & Alley, 2005; Rott et al., 2002). The West Antarctic Peninsula (WAP) also contains hundreds of marine-terminating glaciers, the majority of which are retreating, with the potential to further raise global sea level (Cook et al., 2016; Huss & Farinotti, 2014). The ice shelf and glacial melting have been attributed to an increased intrusion of warm, saline Circumpolar Deep Water (CDW), which originates in the mid-layers of the Antarctic Circumpolar Current (ACC; Cook et al., 2016; Jacobs et al., 1996). Off

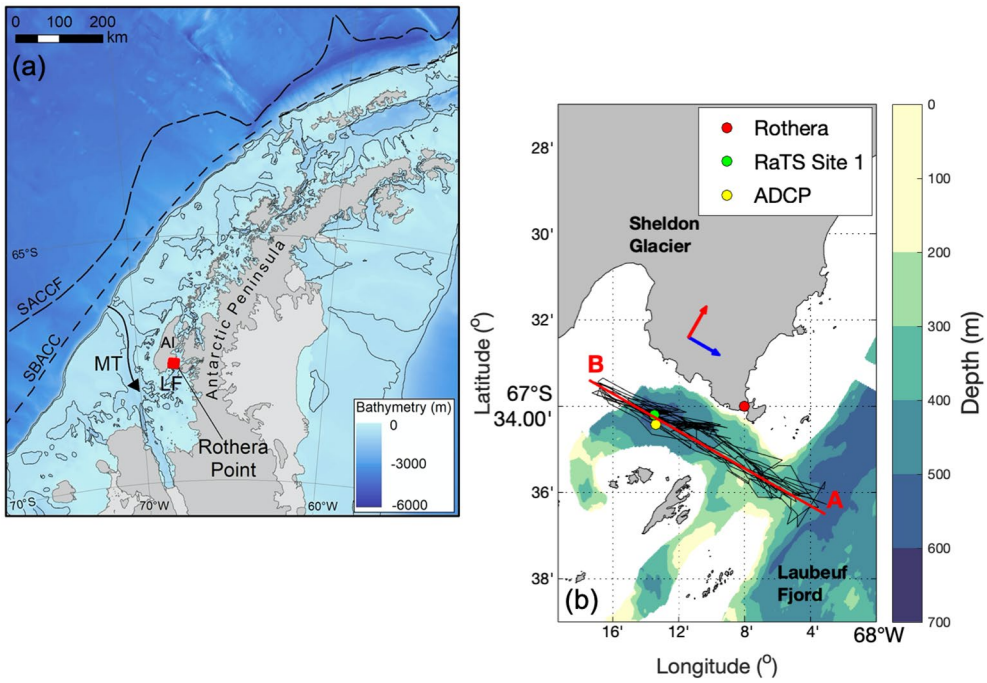

Figure 1. (a) Location of Rothera Research Station on the West Antarctic Peninsula. Marguerite Trough (MT), Adelaide Island (AI), and Laubeuf Fjord (LF) are also indicated. 500 and 1,000 m isobaths from the International Bathymetric Chart of the Southern Ocean (IBCSO) are shown. Dashed black lines indicate the South Antarctic Circumpolar Current Front (SACCF) and Southern Boundary of the ACC (SBACC) from Orsi et al. (1995). (b) Map of Ryder Bay, showing the location of Rothera in relation to the glider tracks. For legibility, only glider data with quality-controlled dissipation estimates are shown. Colors represent quality-controlled bathymetric data (Fremand, 2020), with unsurveyed areas in white. The locations of the Rothera Time Series (RaTS) Site 1 and the ADCP mooring are indicated. Glider data are collapsed onto the A-B transect (red line). Blue (alongshore) and red (cross-shore) arrows show the orientation of the rotating reference frame.

West Antarctica, the southern boundary of the ACC is located close to the shelf break (Orsi et al., 1995), promoting the exchange of CDW onto and across the continental shelf, and providing a source of heat to the base of the ice shelves. Direct inflow through cross-shelf troughs, shedding of eddies from the ACC, and Ekman-induced upwelling, are all thought to be important in conveying CDW onto the shelf (e.g., Arneborg et al., 2012; Martinson & McKee, 2012; Moffat et al., 2009). Once on the shelf, the fate of the CDW heat is controlled by spatially and temporally varying processes (Martinson et al., 2008), such as advection, vertical and horizontal mixing, and heat exchange between the ocean and the atmosphere (Turner et al., 2013). These processes define the components of the WAP oceanic heat budget (Moffat & Meredith, 2018).

The WAP heat budget remains poorly constrained, mainly due to a lack of measurements of vertical mixing and heat flux in the partially ice-covered ocean. However, several studies have produced indirect estimates of various components of the system. Howard et al. (2004) used a Richardson number-based parameterization to infer vertical diffusivities of $<1 \times 10^{-5}$ m^2 s^{-1} from conductivity-temperature-depth (CTD) and acoustic Doppler current profiler (ADCP) data in Marguerite Bay, south of Adelaide Island (Figure 1a), with an associated upward heat flux of <2 W m^{-2}. Similarly, small upward heat fluxes of $\sim$1 W m^{-2} were inferred in Ryder Bay, on the south-east coast of Adelaide Island, using a finescale parameterization applied to CTD and ADCP data (Brearley et al., 2017). However, as the authors acknowledge, the use of such parameterizations introduces a large element of uncertainty, so our understanding of the processes that cause vertical mixing on the WAP remains incomplete. This aside, the vertical heat fluxes inferred by these authors are of a comparable magnitude to the characteristic vertical heat flux associated with the interaction of CDW with ice shelves ($\sim$8 W m^{-2}; Jenkins & Jacobs, 2008), and are therefore considered significant for the WAP heat budget.

One source of vertical mixing in polar environments is double-diffusive convection, where cold, fresh water overlies warm, saline water (Huppert & Turner, 1981). This forms thermohaline staircases with quasi-homogeneous layers separated by strong density gradients, which are identifiable in CTD or microstructure profiles. Double diffusion is generally thought to be important in both the Arctic (Padman & Dillon, 1987) and the Antarctic (Muench et al., 1990; Robertson et al., 1995), where the conditions favorable to its development typically occur. However, on the western side of the WAP, the double-diffusive contribution to vertical mixing appears to be small (Brearley et al., 2017; Howard et al., 2004), despite Turner angles (Ruddick, 1983) being apparently conducive to double-diffusive activity.

A second potential mixing mechanism is via wind-driven near-inertial waves, which, upon breaking, produce shear-driven turbulence. Winds impart momentum to the surface layers of the ocean, forcing near-inertial shear into the water column, with Howard et al. (2004) concluding that this mechanism provided most of the observed shear across the pycnocline in Marguerite Bay. Brearley et al. (2017) also suggested that wind-driven baroclinic waves are the dominant source of shear in the summer months in Ryder Bay, when the region is not covered by sea ice. Other types of internal waves that are typically driven by winds include coastal-trapped waves (CTWs; Allen, 1975) and basin-scale wave modes (Arneborg & Liljebladh, 2001). These processes are thought to be important in Arctic fjordic systems (e.g., Fraser et al., 2018; Inall et al., 2015) and could therefore also be important in analogous embayments on the WAP.

Winds can also influence the WAP heat budget by driving Ekman upwelling/downwelling at the coast: if the orientation of the winds is in the alongshore direction, Ekman transport will drive water toward or away from the coast (Mitchum & Clarlymake, 1986). This process is thought to be significant within Ryder Bay, where wind-induced oscillations of the water column's hydrographic structure are observed (Wallace et al., 2008), causing vertical migration of the interface between CDW and the overlying cold Winter Water (WW). As summer progresses, the upper layers are heated by insolation, and there is an input of fresh meltwater from nearby glacial runoff and sea ice melt. This leads to an increase in stratification and inhibits vertical mixing. In addition, during winter, fast-ice (immobile sea ice that is connected to land) within Ryder Bay hinders the transfer of momentum between the atmosphere and the ocean, thereby reducing the influence of the wind on vertical mixing (Venables & Meredith, 2014). At this time, there is a shift to internal tides as the dominant source of shear (Brearley et al., 2017; Hyatt et al., 2011), highlighting the central role of sea ice as a controlling influence on the WAP oceanic heat budget.

Beneath the ocean's upper layers, the breaking of internal waves over rough topography can lead to enhanced vertical mixing at depth (e.g., Polzin et al., 1997). Internal tides are a primary source of such vertical mixing, transferring energy from barotropic to baroclinic motions (Stigebrandt, 1999) and thus enhancing shear and mixing. Despite barotropic tides being weak along much of the WAP margins ($\leq$3 cm s^{-1}), multiple internal tide generation sites are thought to exist close to Ryder Bay (Wallace et al., 2008). Since the bay is located poleward of the critical latitude for free propagation of diurnal tides, these internal waves dissipate and break locally, generating vertical mixing and upward heat fluxes between CDW and near-surface water masses.

In certain oceanographic contexts, topographic ridges can also lead to enhanced mixing due to the formation of hydraulic structures (e.g., Farmer & Denton, 1985; Farmer & Dungan Smith, 1980; Gregg & Klymak, 2014; Klymak & Gregg, 2004; Legg & Klymak, 2008). A hydraulic structure may form when a stratified fluid flows sufficiently rapidly over topography to arrest the upstream propagation of interfacial waves, resulting in an asymmetric steady-state flow field (Farmer & Denton, 1985) with a transition from sub-critical (slow) upstream to supercritical (fast) flow over the topography (Armi, 1986). While classical hydraulic theory suggests that hydraulic structures are formed when sub-inertial flow moves over ridges, tidal flow is also thought to result in hydraulic conditions with vigorous turbulent dissipation at rates exceeding background levels by several orders of magnitude (e.g., $O(10^{-4})$ W kg^{-1} compared to $O(10^{-7}) - (10^{-8})$ W kg^{-1}; Klymak & Gregg, 2004). Such dissipation bursts can arise due to an increase in flow speed over the ridge, and a sudden decrease in flow speed downstream in a hydraulic jump (Farmer & Denton, 1985). Owing to a large number of ridges present off the WAP, and the occurrence of vigorous sub-inertial eddy flows (e.g., Moffat et al., 2009), flow that is controlled hydraulically may also be an important driver of vertical mixing.

The data analyzed in this study were collected in Ryder Bay, an embayment on the southeast coast of Adelaide Island on the WAP (Figure 1a). The bay is bounded to the north by Sheldon Glacier, which is a marine-terminating glacier that is retreating (Cook et al., 2005), to the west by two smaller marine-terminating glaciers, and to the south by a series of small islands that form a ~300-m-deep shelf (Figure 1b). The deepest part of the bay is ~520 m, and its entrance is marked by a ~300-m-deep ridge separating the bay from Laubeuf Fjord (LF). LF is an ~800-m-deep channel connected via several topographic constrictions to Marguerite Trough (MT), a glacially carved feature with a maximum depth of 1,440 m that extends from the shelf break to the George VI Ice Shelf (Livingstone et al., 2013). MT therefore provides an access route for CDW to flow onto and across the shelf (Klinck et al., 2004), and through LF toward the coast. LF, MT, and the channel connecting them contain multiple transverse ridges that are potential sites for vertical mixing. Underwater gliders deployed in MT have provided data with high spatial resolution and revealed evidence of localized vertical mixing of CDW over these ridges (Venables et al., 2017). The ridges block the densest waters, and as the overflowing water descends hundreds of meters, it entrains the cooler, fresher, but seasonally varying overlying Antarctic Surface Water (AASW).

The close proximity to marine-terminating glaciers and the presence of the ridge make Ryder Bay a fitting locality to study vertical mixing processes and their contribution to closing the WAP heat budget. Here, we investigate the spatiotemporal controls on vertical mixing within Ryder Bay's basin and over the ridge, using some of the first direct estimates of dissipation of the WAP from a glider equipped with a microstructure (MicroRider) package, alongside ancillary CTD, ADCP, and wind data. In Section 2, we introduce the data and methods used to assess the vertical mixing processes. Section 3 describes the mean hydrographic and dissipation patterns observed within Ryder Bay, and documents their temporal variability. In Section 4, we discuss the mechanisms underpinning this temporal variability, explore their relative importance, and evaluate the wider implications of our findings.

2. Data and Methodology

2.1. Glider and Rothera Time Series Hydrographic Data

CTD data were acquired using a 1,000-m-rated Teledyne Webb Research Slocum glider equipped with a pumped Seabird SBE-41 sensor. The glider was deployed/recovered multiple times in Ryder Bay between 11 January 2016 and 1 March 2016, using a rigid inflatable boat that operates out of the British Antarctic Survey's Rothera Research Station. Here we focus predominantly on the last 9 days of the deployment period, between Days 40–50 (20 − 29 February 2016), when the glider recorded 12 repeat transects (Figure 1b). The transects span both the bay's deep region (~520 m) and the topographic ridge (~320 m) that separates the bay from the upstream LF.

Throughout the deployment, the glider's CTD was switched off every other yo (downcast-upcast cycle), so the influence of the pumped CTD on the glider's microstructure data could be assessed (although it was believed that CTD pump noise could affect the shear spectra, no systematic differences were observed). This produced profiles with glider depth but missing CTD data. Consequently, CTD data from the nearest-available adjacent profiles with recorded data were linearly interpolated onto the depths of the missing profiles, and mean interpolated CTD profiles were calculated. When a missing profile was deeper than the immediately adjacent profiles, up to four additional sets of adjacent profiles were searched for data at those depths. The validity of this technique was examined by using the interpolated CTD profiles to reconstruct and compare to all of the recorded CTD profiles. This gave an overall mean root-mean-square error of 0.047°C. This is deemed acceptable, since it causes a <1% difference in the calculation of kinematic viscosity and the dissipation estimates of turbulent kinetic energy (which use the viscosity, Lueck et al., 2002; Wolk et al., 2002).

Using data below 250 m, where the temperature-salinity relationship is most stable, two glider temperature and salinity profiles were compared with concurrent profiles from the RaTS, which aims to sample twice a week in summer (weekly in winter) using a hand-winched SBE-19 pumped CTD package at Site 1 (Figure 1). Estimates for the accuracy of the RaTS temperature and salinity data are 0.002°C and 0.005°C, respectively (Venables et al., 2013). Although discrepancies in temperature-depth profiles were as large as ~0.02°C, they were not systematic, and appeared to be due to isopycnal heave. Consequently, the discrepancies are assumed to be caused by differences in location between profiles, and no temperature adjustments

were made. Sorting the temperature profiles from lowest to highest, and interpolating onto a temperature grid, revealed a consistent salinity offset of 0.0084 g kg^{-1}. This exceeds the accuracy of the RaTS CTD sensor, so a constant offset was applied to correct the glider salinity data.

All hydrographic transects (e.g., Figure 3a) in the following sections are constructed using Laplacian-spline interpolation. The mean and individual transects use a vertical grid spacing of 5 m, and respective horizontal grid spacings of 0.75 and 0.25 km. The mean section requires a larger horizontal grid spacing to smooth the section, which is otherwise noisy due to the high number of observations within each grid cell. The horizontal grid spacing for the individual transects is smaller than the horizontal distance covered by the glider during a profile (~1 km), thereby ensuring that detail is not lost. The horizontal distance is relative to location A along the transect from A to B (Figure 1b). Glider data were collapsed onto this line, which was composed of 100 points with a 0.12 km spacing, by finding the closest point to the location of the data.

2.2. Glider Microstructure Data

The Slocum glider was equipped with a Rockland Scientific MicroRider-1000 with four (512 Hz) microstructure probes installed—two thermistor probes and two orthogonally placed shear probes (shear-1 and shear-2), which can provide estimates of the rate of dissipation of turbulent kinetic energy, ϵ. Essential to the calculation of ϵ is the along-path velocity of the glider, U, as it is used in the conversion of raw shear data into physical units (Lueck, 2016). U is calculated here in a similar way to Schultze et al. (2017), following

$$U = -\frac{w}{sin\left(\frac{\gamma\pi}{180}\right)}, \tag{1}$$

where w is the glider vertical velocity (m s^{-1}) and γ is the glide angle (°): $\gamma = \theta + \alpha$, with θ defining the glider's pitch and α its angle of attack (AOA). Merckelbach et al. (2010)'s hydrodynamic flight model assumes a steady-state flight, and uses the glider's in situ density, buoyancy change, and pitch to produce calibration parameters and generate AOAs. The AOA must be accounted for to avoid a 10% overestimation of the glider's speed (Merckelbach et al., 2010; Schultze et al., 2017). The equation for AOA (Merckelbach et al. (2010); Equation 12) uses the hull lift coefficient, which has previously been a large source of uncertainty, with typical values of 2.4 rad^{-1} being used (e.g., Palmer et al., 2015; Peterson & Fer, 2014). Merckelbach et al. (2019) have recently calibrated the flight model to gain a better estimate of the hull drag coefficient, and so here a value of 3.8 rad^{-1} is adopted, yielding a mean drag calibration coefficient of 0.29 rad^{-2} and a mean AOA of 3.5°. The latter is close to the expected value of ~3°. Our drag calibration coefficient is higher than the ~0.15 rad^{-2} reported by Merckelbach et al. (2019). However, unlike in their study, we used a microstructure probe guard to prevent damage to the probes, and this is thought to significantly increase the glider's drag.

The flight model ingests raw CTD files, so the AOAs and corresponding along-path velocities generated for the missing CTD profiles required correction. Consequently, AOAs for missing upcasts (downcasts) were interpolated from adjacent upcasts (downcasts), in a similar way as the CTD data (flight quality can differ between the two). Up to seven profiles were searched; a comparatively large number because the modeled AOAs are less likely than the CTD data to change in time (upcast/downcast mean and standard errors for the recorded profiles' AOAs are 3.68/− 2.78 ± 0.04/0.04°). Once the AOAs have been interpolated, AOAs calculated <20 m from either end of the profiles are removed, because erroneous values are generated when the glider turns. The AOAs are then used in conjunction with the glider's pitch and vertical velocity to recalculate the along-path velocity of the glider (Equation 1). Comparison of "real" and reconstructed AOAs and speeds gave root-mean-square errors of 0.4° and 0.005 m s^{-1}, respectively, corresponding to ~5%–9% differences in dissipation estimates. This is acceptable, given that dissipation estimates vary by several orders of magnitude.

Once the shear data are converted into physical units using the glider's along-path velocity, spectral analysis is performed to produce shear spectra in the wavenumber domain, $\phi(k)$. The conversion of the shear spectra from the frequency domain to the wavenumber domain is facilitated by adoption of Taylor's frozen turbulence hypothesis, which assumes that the temporal rate of change is less significant than spatial variability. Dissipation estimates are calculated by integrating $\phi(k)$ using

$$\epsilon = \frac{15\nu}{2} \int_{k_{min}}^{k_{max}} \phi(k)\, dk, \tag{2}$$

where $\frac{15}{2}$ is a scale factor accounting for the assumption of isotropic turbulence, ν is the kinematic viscosity of seawater (1×10^{-6} m^2 s^{-1}), and k_{min} and k_{max} are the minimum and maximum limits of integration, respectively (Lueck et al., 2002; Wolk et al., 2002). k_{min} is the lowest possible wavenumber and k_{max} is refined through an iterative process, such that the shear spectra best fit empirically derived Nasmyth spectra (Nasmyth, 1970) describing the expected shear spectral shape for a given dissipation rate (Lueck, 2013; Wolk et al., 2002). This approach is useful to eliminate the parts of the shear spectrum contaminated with instrumental noise. Each shear probe record is divided into 64 s segments that have a 50% overlap, leading to dissipation estimates being calculated every ~7 m horizontally and ~5 m vertically. Fast Fourier transform lengths of 6 s are used, with each transform segment also having a 50% overlap using a cosine tapered window. This incorporates 20 dissipation estimates into each ensemble average estimate, providing 40 degrees of freedom (see Lueck [2013] for details). This process is repeated for each shear probe.

The quality of each shear spectrum is assessed using an automated multi-stage quality assessment algorithm (QAA; see supporting information S1). This was created because a comprehensive assessment revealed that several spectra were contaminated with a 1–3 Hz noise peak, believed to be related to motion of the glider resulting from the relative low H-moment of the vehicle (see supporting information S1 for details). This affected both shear and accelerometer spectra, and whilst the Goodman coherent noise reduction algorithm (Goodman et al., 2006) was able to remove many of these coherent peaks, there were also many instances where residual noise remained in the shear spectrum after the algorithm's application. Consequently, the QAA was designed to remove a peak from the shoulder of a shear spectrum if the Goodman algorithm was unsuccessful. Subsequently, second-order polynomials fitted to both the shear and corresponding Nasmyth spectra were compared to assess whether the observed spectrum had the correct shape. Final dissipation estimates within a profile depend on the percentage of accepted shear-1 and shear-2 spectra within that profile. If either shear-1 or shear-2 contains less than 30% of accepted spectra, then data from that probe are ignored for that profile. For profiles that have over 30% accepted spectra from both shear probes, a mean log_{10} of the two dissipation estimates was calculated. Taking the mean log_{10} of dissipation estimates is typically necessary to avoid mean values being dominated by high values in a log-normal distribution. Ultimately, this method has a negligible impact on the final dissipation estimates in this study because the shear-1 and shear-2 estimates are close together. However, the method was used here to ensure consistency with mean values reported elsewhere in this study. Dissipation estimates from both probes were always used where possible, unlike Schultze et al. (2017), who used the estimate from one probe if the shear-1/shear-2 ratio was greater than 4. This was not deemed necessary here, since the median shear-1/shear-2 ratios from the pre- and post-quality controlled datasets were only 0.65 and 0.7, respectively. Profiles containing less than 30% of accepted spectra in both shear-1 or shear-2 were not used. Despite taking this extra precaution, a comparison of the overall mean vertical profiles of dissipation using no threshold for removing the profile altogether and 30% and 50% thresholds, suggests that the difference is relatively small (all of the 90% boot-strapped error bars overlapped). Using these somewhat conservative criteria, 26% of the dissipation estimates were of good quality, and are considered in this study. The high percentage of rejected spectra stems from Ryder Bay being typically a low-dissipation environment, with dissipation rates close to the noise floor of the instrument, leading to flat spectra that did not clearly agree with the Nasmyth spectra. However, excluding profiles with <30% of accepted spectra resulted in rejection of a further 10% and 7% of the overall shear-1 and shear-2 spectra. Additionally, 11% of the overall shear-1 and shear-2 fell within <20 m from either end of profiles, and were rejected to remove noise contamination associated with glider turning.

2.3. Acoustic Doppler Current Profiler Data

ADCP data were obtained from a mooring deployed in Ryder Bay between 23 January 2016 and 11 January 2017, ~1 km to the south-east of Site 1 at 67° 34.44′S and 68° 13.38′W (Figure 1). The RDI Workhorse Long Ranger, 75-kHz upward-looking ADCP was deployed at a depth of 476 m, 18 m above the bottom (494 m). Horizontal u and v velocities were recorded every ~16 m and 30 min; starting at 451 m to remove

the ADCP's blanking distance, this produces a total of 29 bins. The top depth bin contained extremely high velocities that dominated the barotropic signal, and that most likely resulted from contamination by reflections at the surface. Consequently, the top bin was discarded and velocities were interpolated onto a grid with depths of 25 m and then every 50 m between 50 and 450 m. Data points with a percentage good of less than 50% were also removed, and an offset of − 20° was applied to correct for magnetic declination. ADCP velocities are rotated − 30°, to derive the along-shore u' and cross-shore v' velocities, with positive u' and v' corresponding with flow out of the bay (south-east) and toward the north-east, respectively.

2.4. Rothera Meteorological Data

Year-round, hourly wind speed and direction data are collected at Rothera Research Station, ∼4 km to the north-east of the ADCP mooring location. Wind speed and direction data (recorded at 10 m above sea level) are converted into eastward and northward wind components, and used to calculate τ_x and τ_y wind stress components following Equation 3:

$$\vec{\tau} = \rho_a C_d \overrightarrow{U_{10}} \mid \overrightarrow{U_{10}} \mid, \tag{3}$$

where $\vec{\tau} = (\tau_x, \tau_y)$, $\rho_a = 1.3$ kg m^{-3} is the density of air, $\overrightarrow{U_{10}} = (u, v)$ is the 10 m wind stress vector velocity, and C_d is the drag coefficient. Wind speed is originally recorded in knots, so values are multiplied by 0.51444 to convert to m s^{-1}. The value of C_d chosen varied depending on wind speed, following Trenberth et al. (1990). Wind stress is rotated by −30°, to infer along-shore $\tau_{x'}$ and cross-shore $\tau_{y'}$ wind stress components, with positive $\tau_{x'}$ and $\tau_{y'}$ oriented out of the bay (southeastward) and toward the northeast, respectively. Wind direction is defined relative to the $\tau_{x'}$ axis, with positive values indicating rotation in the clockwise direction.

3. Results

3.1. Mean Hydrographic and Dissipation Patterns

A conservative temperature-absolute salinity plot using data from the entire glider deployment (Figure 2a) reveals the presence of three major water masses. At the surface (<50 m), fresh (∼<33.25 g kg^{-1}), low-density (<26.75 kg m^{-3}; Figure 2b) AASW exhibits a wide range of temperatures (∼− 0.75°C to −2.25°C), and is strongly modified by surface forcing. At depths of ∼50 m lies WW, with temperatures between ∼−1°C and − 1.44°C, close to the freezing point. This approximately coincides with the depth of maximum stratification (60 m; Figure 2b). The water with the highest salinity (>34.7 g kg^{-1}), density (>27.7 kg m^{-3}), and temperature (1 − 1.5°C) is CDW. Located below ∼200 m, CDW has been strongly cooled and freshened relative to its unmodified form in the open Southern Ocean (Venables et al., 2017).

A mean temperature section for the entire glider deployment (Figure 3a) shows the spatial distribution of these water masses. A ∼50 m thick layer of AASW lies in the upper portion of the water column, above a thin (20 − 30 m thick) layer of very cold WW. The WW forms as a thick homogeneous mixed layer in winter, and is gradually warmed from above during the summer months via short-wave solar radiation, and from below by mixing with CDW. The main thermocline has a mean depth of 130 m, and is defined here using the 0.25°C isotherm, following the representative isotherm method (Fiedler, 2010). A seasonal thermocline is observed close to the surface at a distance of ∼4 km from A, where temperatures reach ∼1.5°C at the surface, thereby increasing upper-ocean stratification. Below the main thermocline, CDW extends to the seafloor. The warmest (1.5°C) CDW is blocked by the ∼150 m topographic ridge that separates Ryder Bay's deep basin (∼520 m) from LF. Above the thermocline, the mean isopycnals are predominantly flat and show a greater change in density with depth than those below the thermocline, where changes in density are more subtle. The densest isopycnal (27.74 kg m^{-3}) deepens in the distance range of 6 − 8 km, before shoaling again after 8 km in the inner part of the bay. The presence of warm CDW at depth means that there is a reservoir of heat available that can be mixed into the overlying WW and AASW. We will quantify such heat fluxes through our calculations of temperature gradients and ϵ.

A section of mean ϵ reveals significant spatial variability within Ryder Bay (Figure 3b). Although the top 20 m are removed due to pitch motor noise from the glider turning, elevated dissipation rates $O(10^{-8})$ W kg^{-1}

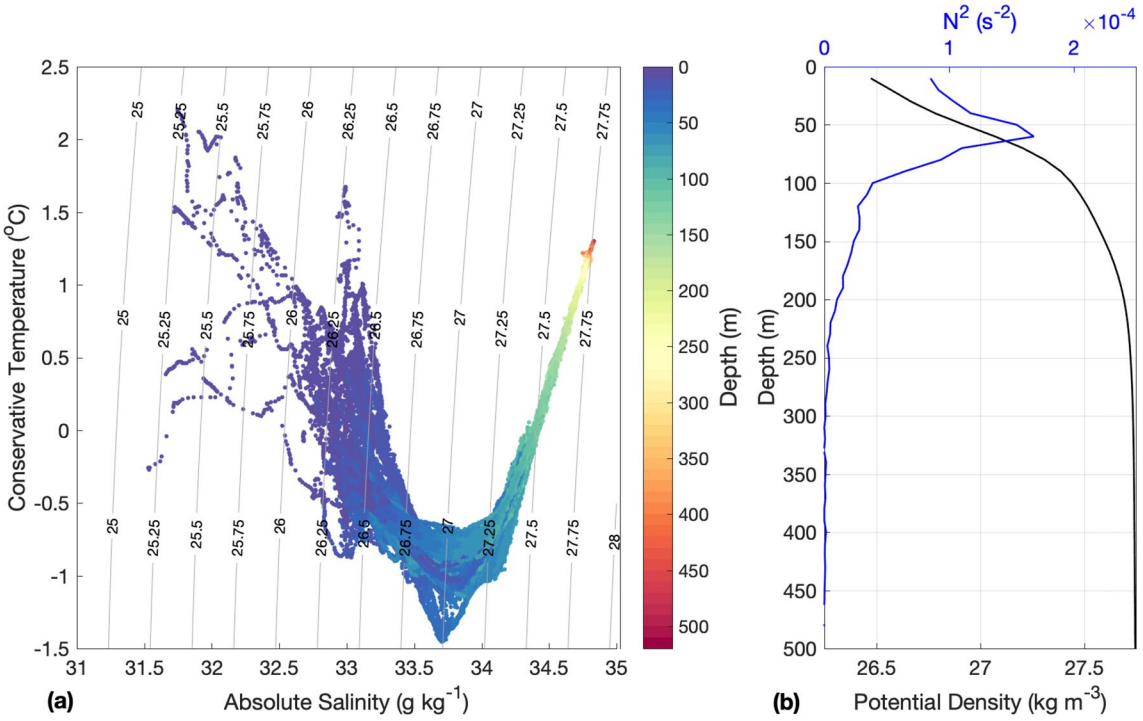

Figure 2. (a) Conservative temperature-absolute salinity diagram, using data from the whole glider deployment and colored by depth. Potential density contours (−1,000) between 25 and 28 kg m^{-3} are shown. (b) Mean glider profiles of the Brunt-Vaisala frequency squared, N^2, and potential density (−1,000 kg m^{-3}).

are found between 20 and 50 m. This is most likely due to the input of wind energy into the water column, discussed in more detail in Section 3.2.1. In the deep part of the bay, between ~5.4 and 10 km along the baseline, ϵ is very low, $O(10^{-10})$ W kg^{-1}. In contrast, above the ridge, defined here as between 1.3 and 5.4 km, ϵ is significantly higher, particularly below ~200 m, with rates $O(10^{-8})$ W kg^{-1}. The highest dissipation rates at depth are closest to the ridge, implying that the observed spatial pattern is attributable to ridge-flow interaction.

Dissipation rates can be used to quantify the diapycnal diffusivity, κ_ρ, using the Osborn relation:

$$\kappa_\rho = \Gamma \frac{\epsilon}{N^2}, \tag{4}$$

where Γ is the mixing efficiency, taken here to be the typical value of 0.2 (Osborn, 1980), and N is the buoyancy frequency, a measure of the stratification. κ_ρ can be used to quantify the transfer of different properties including heat and salt. Low mean diapycnal diffusivities $O(10^{-6}) - O(10^{-5})$ m^2 s^{-1} are observed in the upper 200 m, where the stratification is higher. Below 200 m, κ_ρ values $O(10^{-4}) - O(10^{-3})$ m^2 s^{-1} are observed, with highest values above the ridge (see Figure S5). This demonstrates that, in the presence of a negative upward temperature gradient, the ridge could cause a significant flux of heat toward the base of the thermocline, where it can be more easily mixed with surface waters through additional mixing processes.

3.2. Observed Temporal Variability

The 12 glider transects reveal significant temporal variability in both the hydrography of Ryder Bay and the turbulent dissipation in the area. Three representative transects are chosen to highlight this temporal variability (Figure 4).

The thermocline in Transect 4 (23 February 2016; Figure 4a) is relatively flat with a mean depth of 143 m. The mean temperature at 200 m is 0.95°C, and the warmest (~1.27°C) CDW does not pass over the first

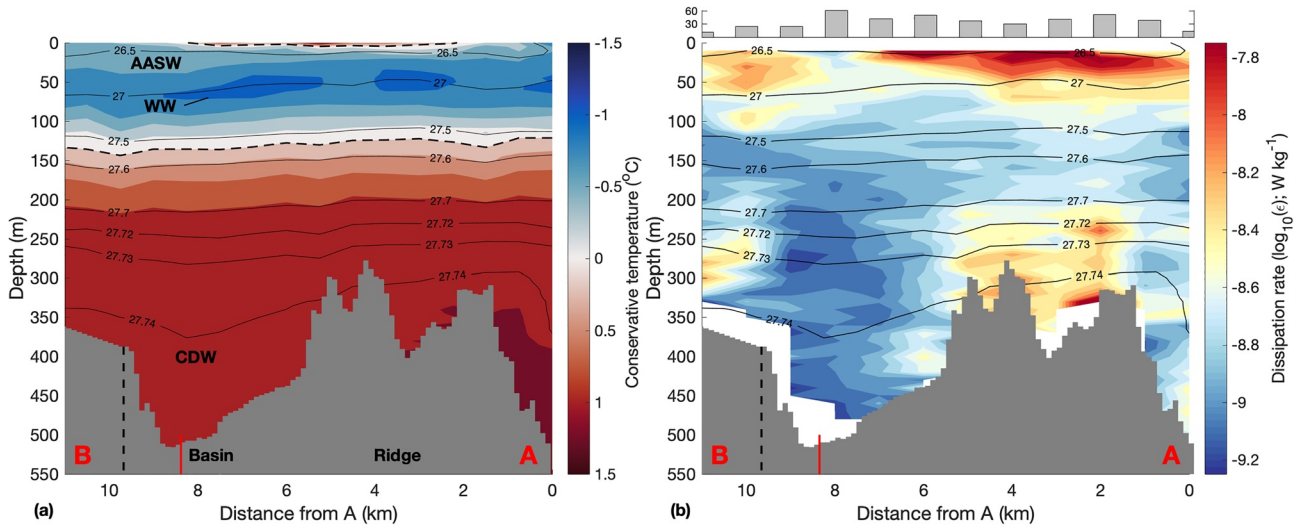

Figure 3. (a) Mean vertical section of conservative temperature (°C). The seasonal and main thermoclines are defined using the 0.25°C isotherm (following Fiedler, 2010), and are indicated using horizontal dashed black lines. Contours are in 0.25°C increments from − 1.25°C to 1.5°C. (b) Mean vertical section of the dissipation of turbulent kinetic energy, ϵ. Prior to plotting, dissipation data were binned into 10 m depth and 1 km distance bins to ensure a sufficient number of data points were averaged into each bin. Contours are in $log_{10}(0.1)$ increments from $log_{10}(-9.5)$ to $log_{10}(-7.5)$ W kg^{-1}. To provide insight into data coverage, the number of different profiles used in each distance bin is shown in the bar chart above the main panel. The ADCP mooring location (vertical red line overlaying the gray bathymetry) and 26.5–27.74 kg m^{-3} isopycnals (black contours) are shown on both vertical sections. Bathymetry is from Fremand (2020) up until ~9.7 km (dashed vertical line), after which no data exists. Therefore, the bathymetry is linearly interpolated up to a depth of 350 m at 12 km along the section.

peak of the ridge. The isopycnals below the thermocline pinch together above the ridge at 5 km along the section, and are steeply sloping in the lee of the ridge, with the densest isopycnals having the greatest slope at respective distance and depth of 5.5 km and 340 m. The densest layers thicken downstream within the basin. Elevated dissipation is observed from the thermocline down to the depth of the ridge, with the largest values $O(10^{-7})$ W kg^{-1} found closest to the ridge.

Transect 10 (February 27, 2016; Figure 4b) has a shallower thermocline that shoals inshore toward B, being located at 90 m between 3 and 10 km, and at ~110 m depth between 0 and 3 km along the section. At 1.09°C, the temperature at 200 m is 0.15°C warmer than in Transect 4, and the warmest CDW layer has passed over the first crest of the ridge (although it has not spilled into the main part of the basin). The isopycnals below the thermocline are similarly arranged to those in the mean section (Figure 3a) but with a shallower, more consistent slope than in Transect 4 between 3 and 9 km. ϵ close to the seafloor shows only a slight increase above the ridge and in the basin, with rates $O(10^{-10})$ W kg^{-1}.

The temperature structure in Transect 12 (February 29, 2016; Figure 4c) is noticeably different from the previous two transects. The thermocline deepens from A (~130 m) to B (~160 m), and the mean 200 m temperature of 0.80°C is 0.30°C cooler than in Transect 4. Unfortunately, the glider did not complete the section between ~0 and 2 km and below ~200 m depth, so the location of the warmest (~1.27°C) CDW cannot be determined. Despite this, CDW appears to have retreated back into LF and failed to cross the first peak of the ridge. Unlike in Transects 4 and 10, where the thickness between the thermocline and the 27.7 kg m^{-3} isopycnal below is relatively constant, in Transect 12, the thickness between these layers ranges from ~75 m at 7.50 km to 130 m at 2.75 km from A. Below ~250 m, the isopycnal layers vary on smaller horizontal scales than in the previous transects, with large changes in thickness and slope along the length of the section (note that the density inversion at 1.75 km and 240 m is an artifact of contouring with shallower glider profiles < 1.75 km). The variability in the thickness of the temperature and density layers suggests that the water in this region was less quiescent during Transect 12. This is consistent with the observed elevated dissipation across the bay, both above and below the thermocline, typically $O(10^{-8})$ W kg^{-1}.

The transects above exhibit three key features: (i) a deepening and shoaling of the thermocline, (ii) basin-wide elevated dissipation within and across the thermocline, and (iii) strongly enhanced (but variable)

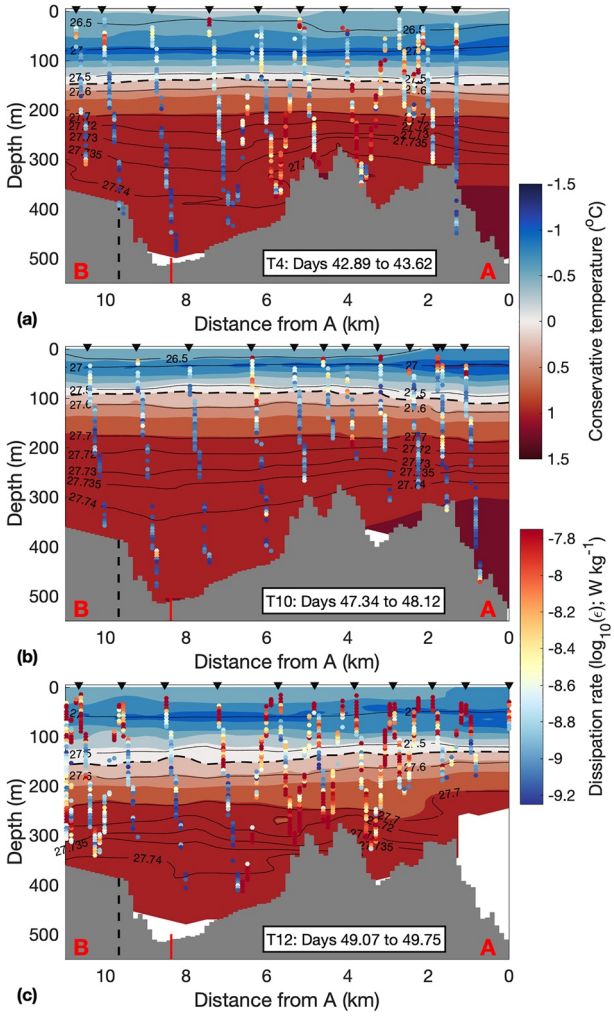

Figure 4. Vertical sections of conservative temperature for Transects 4 (a), 10 (b), and 12 (c), with individual dissipation estimates overlain. Temperature contours are in 0.25°C increments from − 1.25°C to 1.5°C. Dissipation contours are in $log_{10}(0.1)$ increments from $log_{10}(-9.5)$ to $log_{10}(-7.5)$ W kg^{-1}. The black markers indicate the start of each downcast. Dashed black lines denote the thermocline (defined using the 0.25°C isotherm). Black contours indicate the 26.5–27.74 kg m^{-3} isopycnals. (Note that the density inversion at 1.75 km and 240 m is an artifact of contouring with shallower glider profiles <1.75 km).

deep dissipation above the topographic ridge. The physical controls for each of these features are explored in detail below.

3.2.1. Variability in Thermocline Depth

The 0.30°C reduction in temperature at 200 m between Transects 10 and 12, and the observed ~50 m heaving of the thermocline, are most likely caused by changes in wind forcing, which have previously been shown to be important within Ryder Bay (Wallace et al., 2008). During the glider deployment, a range of wind strengths and directions were recorded at Rothera Research Station, and analysis of ERA-Interim meteorological data from the same period (not shown) reveals that this variability is related to a number of cyclonic storms that transited across the region. Wind roses from three important days illustrate the nature of this variability (Figure 5a). Strong winds of >25 m s^{-1} are observed in both the south-westward (e.g., Days 40 and 47) and north-westward (e.g., Day 44) directions. These directions are predominantly cross-shore (red), but do have some along-shore (blue) component (dashed lines in Figure 5a represent the cross-shore/along-shore reference frame). Mean wind directions are calculated for each day since the start of the deployment (Figure 5b) using the method of Berens (2009), which transforms the directions into unit vectors and then vector-averages to produce the mean resultant vector $\overline{r}$ (angles calculated using this method are labeled with a T). Days 40, 44, and 47 are characterized by mean rotated directions of 280°T, 122°T, and 277°T, respectively. The circular variance of wind direction (S), which is given by $S = 1 - \| \overline{r} \|$ (Berens, 2009), is a metric of how variable the wind direction is on any given day. S changes throughout the deployment (Figure 5b): low variances (compared to the 0.36 mean) are observed on Days 40, 44 (0.05), and 47 (0.04), whereas other days experience much larger variability in wind direction (e.g., Day 31 has a variance of 0.85). Days with lower wind speeds typically have higher variances.

The internal Rossby radius of deformation (r_r) provides a characteristic scale over which rotational processes, such as Ekman flow, are likely to be important in a given region, and is calculated using:

$$r_r = \frac{NH}{f}, \tag{5}$$

where N is the buoyancy frequency (with $N^2 = 3.4 \times 10^{-4}$ s^{-2} corresponding to the median maximum stratification from the individual glider profiles), H is the characteristic depth of the pycnocline (50 m; the corresponding median depth), and f is the Coriolis parameter (at 67.58°S, $f = 1.3 \times 10^{-4}$ rad s^{-1}). This gives $r_r = 6.8$ km within Ryder Bay. The width of Ryder Bay is ~4 km, the same order of magnitude as the Rossby radius. The velocities recorded by the ADCP are thus likely to be significantly influenced by Ekman dynamics. Ekman transport is expected to be 90° to the left of the wind direction in the Southern Hemisphere, so daily mean wind directions (Figure 5b) are used to predict Ekman flow directions. Predicted flow directions are compared with 25 m ADCP-derived values (Figure 5c), where that depth is chosen because it is close to the median, glider-derived mixed layer depth (MLD) of 22 m, calculated using a density difference of 0.03 kg m^{-3} compared to the 10 m density. This is thought to be an appropriate comparison, since the Ekman depth is typically similar to the MLD (Thomas & Lee, 2005). Directions ranging from 180° to 360° are converted to values between −180° and 0° to enable ready comparison of angles close to 0°. The jump between expected and observed angles of −180° and 180° on Day 45 is misleading because the converted −180° is the same angle as 180°. Expected and observed flow directions have a correlation of 0.63 ($p \ll 0.001$) with a median absolute difference of 22°. There is no systematic

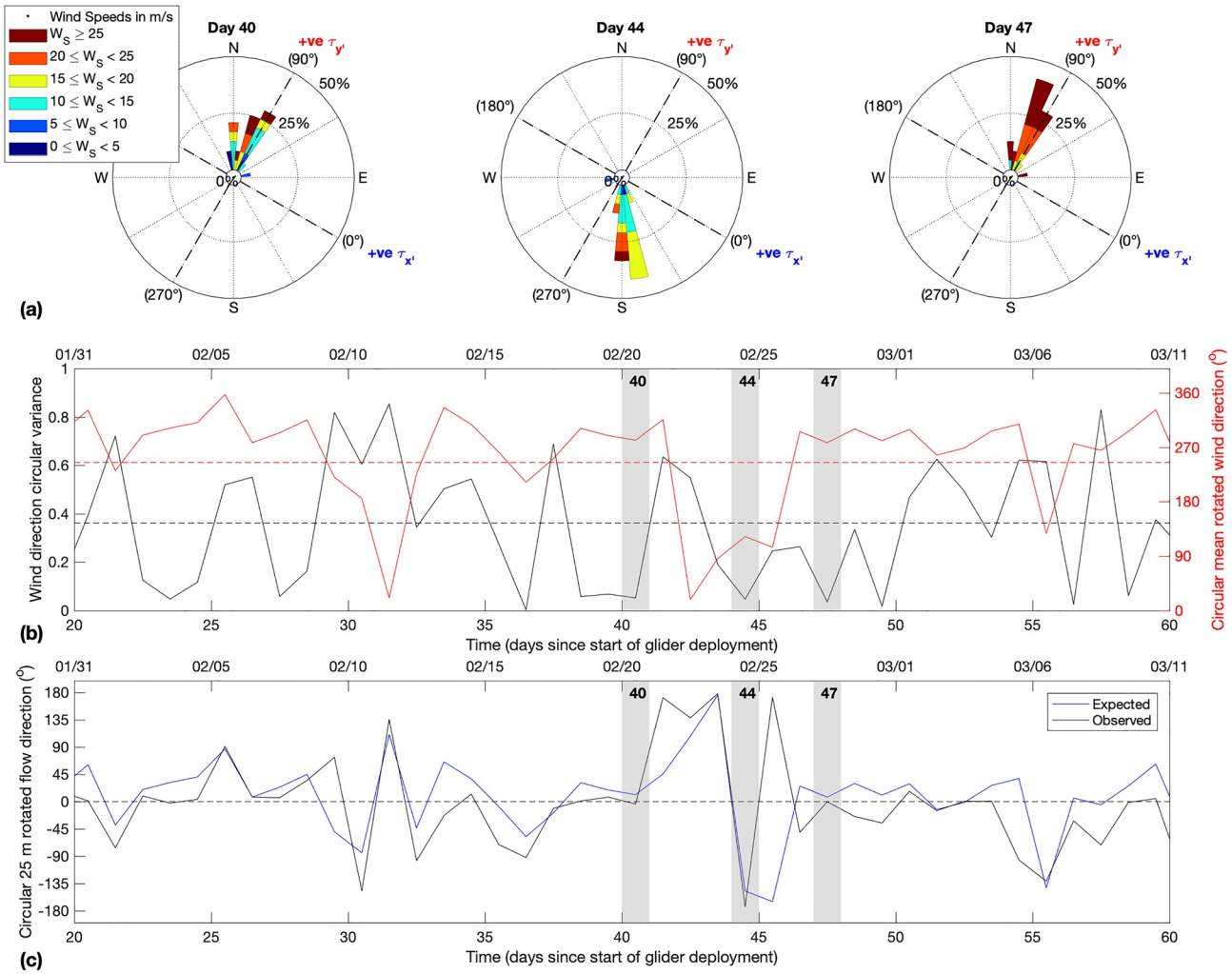

Figure 5. (a) Wind rose plots for Days 40, 44, and 47. The coordinate frame has been rotated by −30°, so that wind directions of 0° and 90° are in the positive $\tau_{x'}$ and $\tau_{y'}$ directions, respectively (Red and blue wind stress labels are for reference when examining Figure 6). (b) Circular variance of wind direction (black solid line) and mean coordinate-rotated wind direction (red solid line). Dashed lines represent the corresponding mean for the first 100 days since the start of the glider deployment, when there is no fast-ice. (c) Comparison of the expected and observed flow directions at 25 m depth, using angles between 0° and ± 180° (see text for details). Days 40, 44, and 47 are highlighted in gray because they are referred to in the text. Date in 2016 is shown along the top (b and c).

difference in the sign of the offset, with positive and negative values occurring 48% and 40% of the time, respectively. Differences likely depend on the strength of the wind and the precise location of the ADCP within the Ekman layer, with stronger winds likely penetrating deeper into the water column and causing smaller directional differences (e.g., 8° on Days 40 and 47) than weaker winds (e.g., − 27° on Day 44).

The importance of Ekman processes is assessed in greater depth using the mixed layer slab model first proposed by Pollard and Millard (1970). This simple model uses MLD (H) and wind stress ($\tau_{x'}$, $\tau_{y'}$) to predict wind-generated flow (Z). The model equation is expressed using complex notation as in D'Asaro (1985):

$$\frac{dZ}{dt} + \omega Z = \frac{T}{H}, \tag{6}$$

where

$$Z = u + iv, \omega = r_d + if \text{ and } T = \frac{\tau_{x'} + i\tau_{y'}}{\rho}.$$

ω and T are the damping/Coriolis and wind stress body force terms, and ρ is the overall mean density of the mixed layer (1,026.53 kg m^{-3} from observations). r_d is an artificial linear Rayleigh damping parameter used as a simple representation of momentum sinks (e.g., including momentum expended in generating internal waves and small-scale turbulence; Mickett et al., 2010). r_d can be used to tune the model and, following Alford (2001), $r = 0.4f$ was chosen here to optimize the correlation between the observed and modeled near-inertial velocities (discussed in Section 3.2.2). The model assumes uniform velocity and density, and realistic simulations require $r_d^2 \ll f^2$ (D'Asaro, 1985) and $r_d > 0$ for stability (Alford, 2001).

The mixed layer model decomposes the overall wind-generated flow into Ekman, Z_E, and near-inertial, Z_I, velocity components using:

$$Z = Z_I + Z_E. \tag{7}$$

Adopting a constant MLD of 20 m (comparable to the shallowest ADCP velocities and the glider-derived MLD of 22 m) and observed wind stress magnitudes, the modeled Ekman velocities are given by Equation 8, following (D'Asaro, 1985):

$$Z_E = \frac{T}{\omega H}. \tag{8}$$

The model sufficiently replicates observed Ekman flows, with a correlation of $R = 0.60$ ($p \ll 0.001$) between modeled and observed values (Appendix A). Observed Ekman velocities were calculated by subtracting the band-pass filtered near-inertial velocities from the total observed velocities, in the same way as in Equation 7. The R^2 value between Z and Z_E ($R^2 = 0.80$) is larger than that between Z and Z_I ($R^2 = 0.44$), suggesting that Ekman processes are important within Ryder Bay (both correlations have $p \ll 0.001$).

A time series of bay-rotated wind stress ($\tau_{x'}$, $\tau_{y'}$) reveals that the cross-shore, south-westward and north-westward winds on Days 40 and 44 are part of strong ~3-day duration wind forcing events (Figure 6a) that have along-shore components that blow out of and into the bay, respectively (positive and negative $\tau_{x'}$). The midpoint of each event lies on Days 39 and 44, so these will be referred to hereafter as Days 39 and 44 events. The events are preceded by a long, relatively quiescent period between Days 29 and 37, are separated by a 2-day-long quiescent period, and are followed by a prolonged period of strong winds that vary on shorter time scales (<2 days) from Day 46 onward (e.g., note the large west/south-westward and southward wind stress peaks on Days 47 and 50, respectively). With Ekman processes likely playing an important role, the potential impact of these wind events on the water column velocities is investigated below.

Mean ADCP velocity profiles for Days 40, 45, and 48 (Figure 6b) are chosen to illustrate how the structure of the water column changed over the period of glider observations. Velocities on day 40 have a dipole structure with a zero-crossing at a depth of ~100 m. The uppermost velocity (25 m), close to the MLD, flows out of the bay in the positive along-shore direction (the expected Ekman transport direction; Figure 5c). Flow rotates to the left with increasing depth, down to the zero-crossing at ~100 m, where the flow is quasi-parallel with the positive cross-shore direction (v'). This is qualitatively similar to an Ekman spiral, but we note that an Ekman depth this deep is unlikely given the mean upper 200 m diapycnal diffusivities of ~10^{-5} m^2 s^{-1}. Ekman-influenced flow can extend up to two times the MLD following strong wind events, as previously observed in the mid-latitude Atlantic Ocean (Chereskin & Roemmich, 1991). This produces a maximum Ekman depth of ~44 m. Velocities between the MLD and ~44 m have a northward component, consistent with Ekman-induced flow toward the northern boundary of Ryder Bay. In the lower layers (below ~150 m), flow is generally uniform, with both negative cross-shore (v') and along-shore (u') components. The orientation of this dipole (with positive cross-shore velocities above the pycnocline and negative below) is consistent with a circulation structure that has upwelling at the southern boundary and downwelling at the northern boundary of Ryder Bay.

The dipole persists for ~4 days until the Day 44 wind event, when the surface flow rotates to an inflowing direction (negative along-shore u') in response to the north/north-westward wind, and there is predominantly negative cross-shore flow (south-westward) in the upper layers (Day 45; Figure 6b). A quasi-barotropic southward velocity structure forms and persists for ~3 days, including strong, negative cross-shore velocities in the upper water column on Day 47 (not shown). On Day 48, the lower-layer velocities switch to

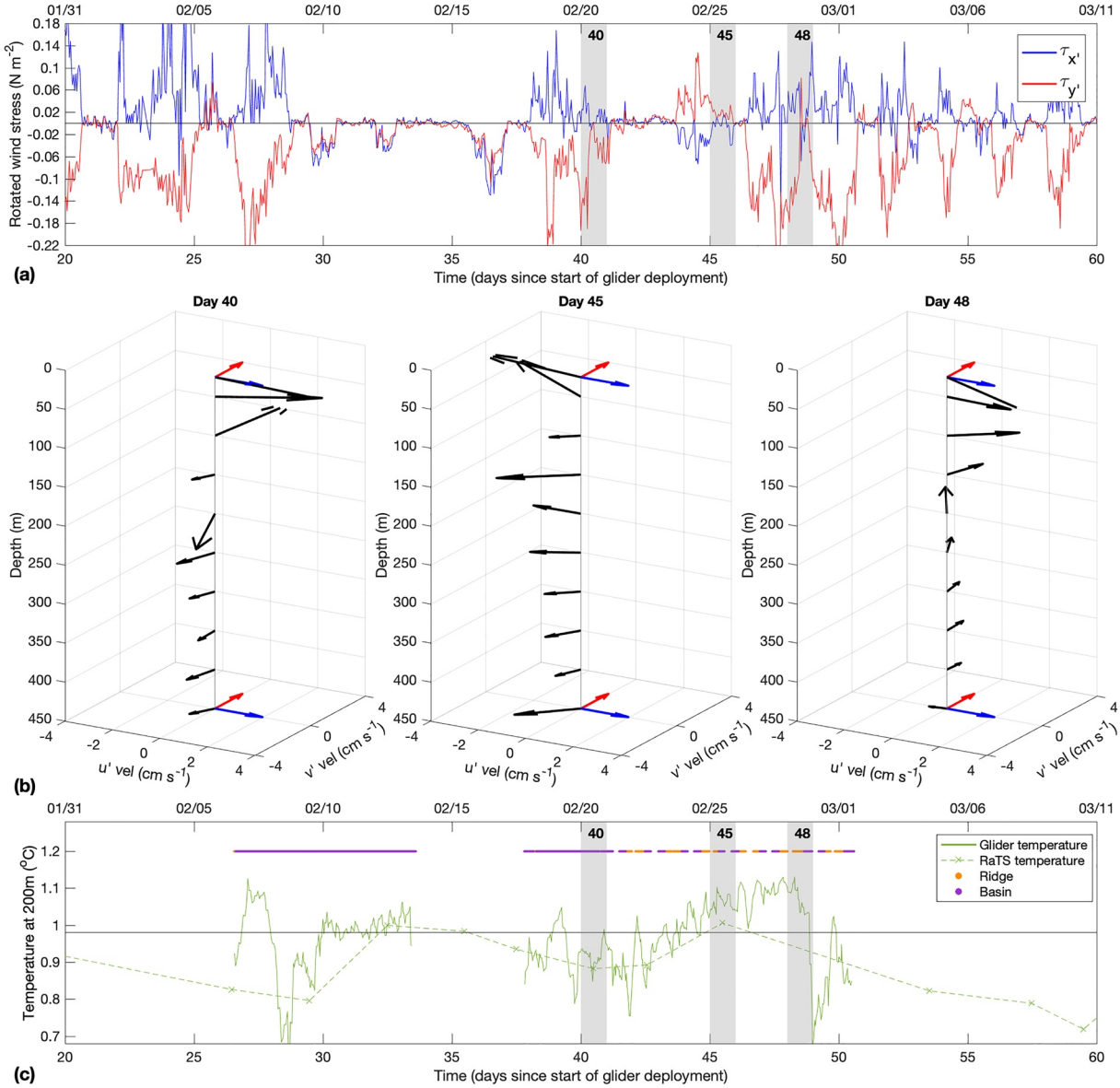

Figure 6. (a) Time series of rotated $\tau_{x'}$ and $\tau_{y'}$ wind stress. (b) Mean ADCP velocities for Days 40, 45, and 48, interpolated onto depths of 25 m and then every 50 m between 50 and 450 m, shown with a three-dimensional perspective. 2 cm s^{-1} in the u' and v' directions are represented by the red and blue scale arrows, respectively. (c) Time series of glider (solid) and interpolated RaTS (dashed; crosses are sample points) temperature at 200 m. The black line at 0.98°C is the overall mean glider temperature, and is used to determine whether or not the temperature is elevated. The orange and purple lines are used to show when the glider is above the ridge or in the basin, respectively. Gray columns show the following days of interest: 40, 45, and 48. ADCP, acoustic Doppler current profiler; RaTS, Rothera Time Series.

a positive cross-shore direction, which is likely a delayed response to the negative cross-shore upper velocities, and reflects a change from wind-induced coastal upwelling to downwelling on Ryder Bay's southern boundary. The positive cross-shore velocities at depth are not sustained in any given direction after Day 48, possibly due to the strong variation in wind direction after Day 46.

If, as argued, the observed velocities are associated with wind-induced coastal upwelling/downwelling, one would expect to see corresponding changes in the glider and RaTS mean 200 m temperature (Figure 6c). The glider data exhibits the same low-frequency variability as the RaTS data, but the increased resolution reveals higher-frequency variability that is not captured by RaTS's sparser sampling (nominally twice a week in summer). Large decreases in temperature of 0.40°C and 0.46°C are observed on Days 28 and 48,

respectively, which coincide with changes between negative and positive cross-shore flow at depth (Day 48; Figure 6b). Both decreases also occur when the glider is in the basin (as opposed to over the ridge), so spatial differences in flow can be ruled out. The mean 200 m glider temperature increases steadily from 0.92°C to 1.06°C between Days 40 and 46, and reaches 1.13°C at the start of Day 48. This coincides with the period of negative cross-shore flow at depth, and upwelling on the southern side of Ryder Bay. On 63% of the days in which the glider recorded an elevated mean temperature, a negative cross-shore flow at depth was recorded on either the same or the previous day. A two-sided Wilcoxon rank-sum test comparing these cases with the full daily mean glider temperature time series (37 days of data between Days 1 and 51) indicates that this observation is statistically significant ($p = 0.015$). This dependence of the 200 m temperature on the flow direction at depth confirms our earlier supposition that flow is largely controlled by Ekman coastal upwelling and downwelling.

3.2.2. Basin-wide Turbulent Dissipation at the Thermocline

There are multiple processes that could be responsible for the basin-wide dissipation event that occurred above and across the thermocline during Transect 12 (Figure 4c). Basin-scale wave modes and CTWs are important in Arctic fjordic systems similar to Ryder Bay (e.g., Fraser et al., 2018; Inall et al., 2015) and were therefore initially considered in this study. Following Fraser et al. (2018), the mode-1 fundamental "quarter pipe" period for Ryder Bay is 19 h. However, spectral and wavelet analysis of barotropic u' (along-shore) velocities revealed no evidence for seiching at this period (not shown). Higher-order modes are less energetic than the fundamental mode (Inall et al., 2014), suggesting that they are also not important within Ryder Bay. Additionally, periods of significant power in the wavelet analysis were likely too broadband to be characteristic of CTWs, which are generally in a narrower range (e.g., 40–60 h; Inall et al., 2014). This points to other processes being responsible for the thermocline dissipation.

Winds are a primary source of near-inertial kinetic energy and shear in the upper water column (D'Asaro, 1985; Wunsch & Ferrari, 2004) and are another mechanism that may have generated the basin-wide thermocline dissipation in Figure 4c. A time series of wind stress magnitude between 20 and 100 days shows multiple strong wind events occurring during the glider deployment (e.g., Days 27, 39, 47, and 50; Figure 7a). Integrated near-inertial shear squared values, U_z^2, within the 105–205 m layer are calculated using 0.9–1.9f band-pass Butterworth filtered ADCP velocities (u_{NI}, v_{NI}) on an hourly time grid (Figure 7b):

$$U_z^2 = \int_{z=105}^{z=205} \left(\left(\frac{du_{NI}}{dz} \right)^2 + \left(\frac{dv_{NI}}{dz} \right)^2 \right) dz. \tag{9}$$

The 105–205 m depth range was chosen to focus on processes occurring across the main thermocline, a region important for the exchange of heat between the CDW and AASW layers. A depth layer definition was chosen instead of a vertical range centered on the 0.25°C thermocline isotherm because the former definition does not require hydrographic data and ensures a continuous integrated shear time series. However, a sensitivity test revealed that differences between shear values generated by these two methods were small. Elevated near-inertial shear is observed on Days 28, 41, 49, and 50 (at similar times to the wind events highlighted above), yet there is no significant correlation between 20 and 100 days unfiltered wind stress magnitude and near-inertial shear squared time series. Applying a 4-day low-pass Butterworth filter to both time series (magenta lines; Figures 7a and 7b) and conducting a cross-correlation analysis reveals that the highest correlations occur when the near-inertial shear lags behind the wind stress by 1.7 days. Accounting for this 1.7-day lag between the low-passed time series gives a correlation of $R = 0.47$ ($p = 2 \times 10^{-3}$), which increases to $R = 0.92$ ($p \ll 0.001$) using only data between Days 30 and 55 (the mixed layer model period, see below). This suggests that winds are an important controlling influence on the shear within the thermocline during the period of our observations.

Comparison of the near-inertial shear with hourly mean dissipation estimates within the 105–205 m layer shows that periods of elevated dissipation coincide with enhanced shear on Days 28, 40, and 48 (Figure 7b). Mean dissipation estimates are linearly interpolated where required; over the zoomed-in period when the glider made multiple transects (Figure 7c), mean dissipation estimates were calculated ~70% of the time (circles), and ~90% of the interpolated gaps were only 1 h long (the maximum interpolated gap length

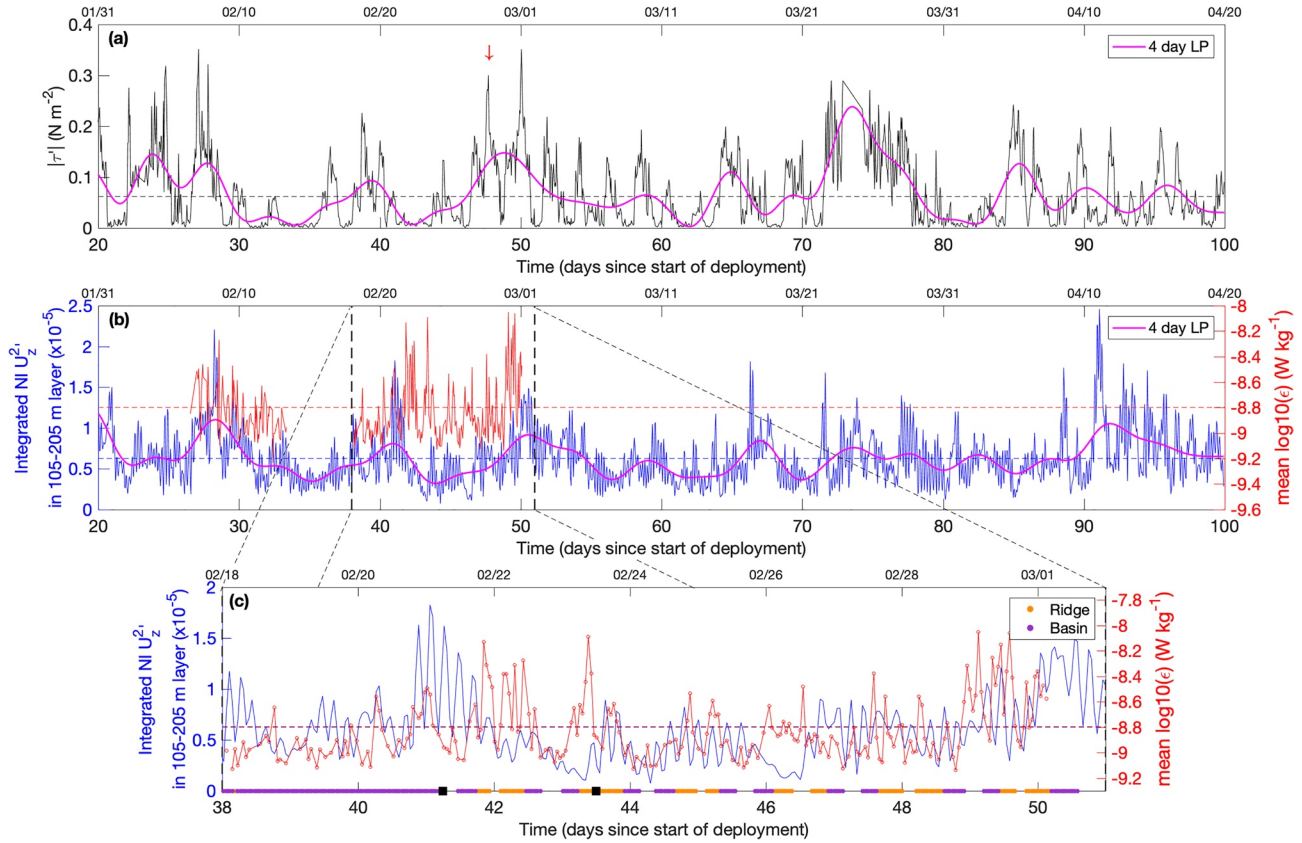

Figure 7. (a) Time series of hourly wind stress magnitude. The magenta line represents the 4-day low-pass Butterworth filtered signal. The red arrow indicates the wind event that likely caused the elevated dissipation in Transect 12 (Figure 4c). (b) Integrated near-inertial (0.9–1.9*f*) shear squared within the 105–205 m layer, with magenta line as in (a). Overlain are interpolated hourly mean dissipation rates. Real dissipation estimates (red circles) occur 70% of the time, with 94% of the gaps being 1 h and a maximum gap of 3 h. Vertical dashed lines indicate the period shown in (c). Black squares show periods considered for correlations. All horizontal dashed lines represent the quantity means between 20 and 100 days; these have been aligned in (c).

over this period was 3 h). The dissipation in Figure 7b is offset vertically from the near-inertial shear to aid visibility of the latter; however, mean near-inertial shear and dissipation values are aligned in Figure 7c (horizontal lines) so that elevated periods are more easily visible. Although periods of low (high) shear appear to coincide with periods of low (high) dissipation, overall there is no statistically significant relationship between near-inertial shear and dissipation between Days 38 and 51. The large differences found between Days 41.25 and 43.50 are likely responsible. The correlations before and after this period are $R = 0.38$ ($p = 0.01$) and $R = 0.24$ ($p = 0.06$), respectively. The statistically significant correlation between Days 38 and 41.25 could reflect the glider maintaining close proximity to the ADCP mooring. The second correlation's statistical significance is marginal at the 5% level, which may initially suggest that other processes could be responsible for the thermocline dissipation. However, as stated above, other candidate processes such as basin-scale wave modes and CTWs are not thought to be important within Ryder Bay. Consequently, some of the differences between near-inertial shear and dissipation could, at least in part, be of spatial origin (with higher dissipation always present over the ridge, where other processes could contribute to the observed dissipation in the 105–205 m layer). Additionally, some periods of elevated dissipation but only moderate near-inertial shear can be attributed to super-inertial energy, which may have either been directly generated by wind events, or transferred from the near-inertial band to higher frequencies through the breaking of internal waves; for example, the elevated dissipation spike at the start of Day 49 (not shown).

The mixed layer slab model introduced above can be used to investigate wind-driven near-inertial motions (e.g., Alford, 2001, 2003; D'Asaro, 1985; Mickett et al., 2010). The simplicity of the model (only requiring two inputs) enables its use as an independent method of estimating wind-generated near-inertial velocities that

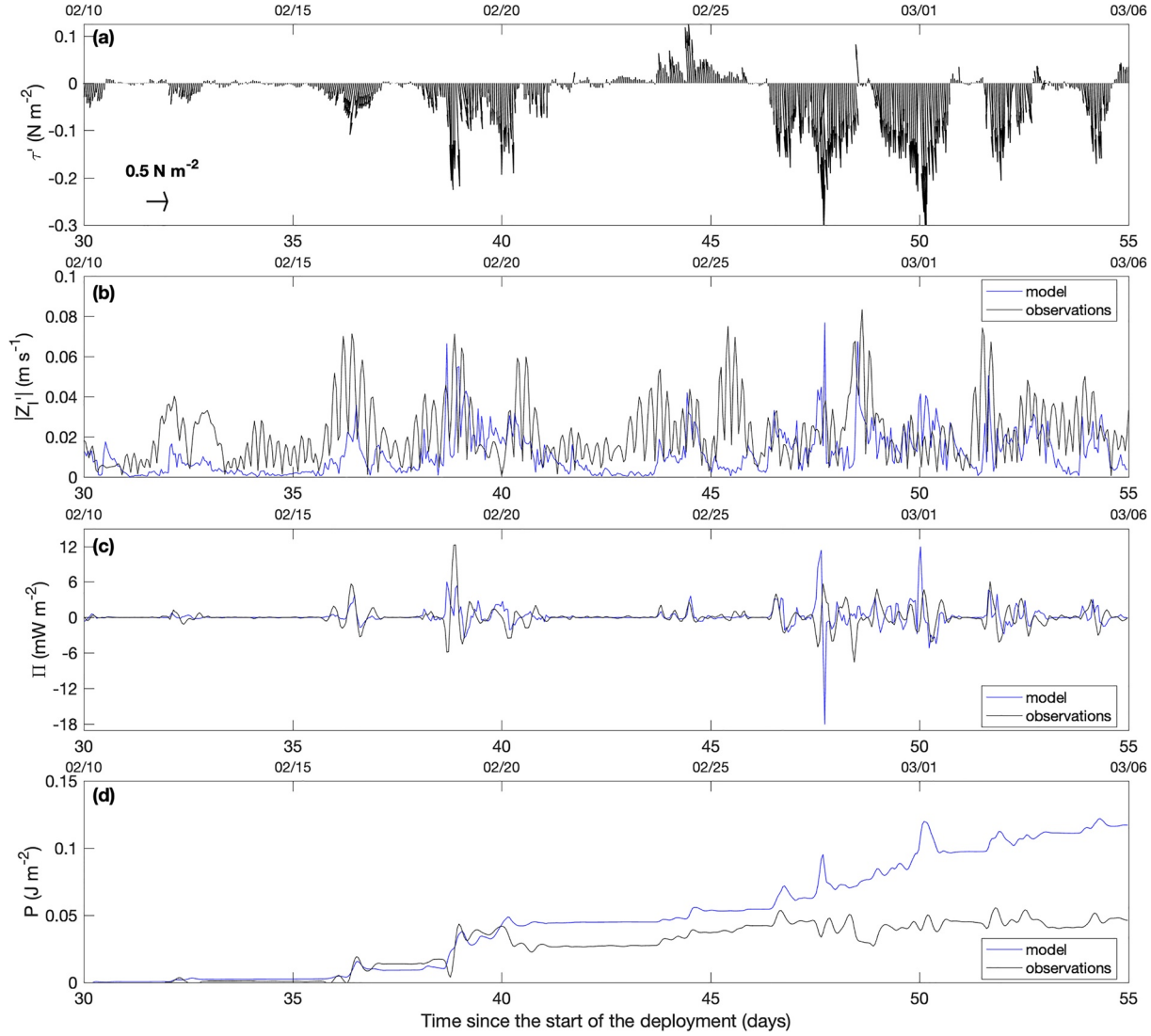

Figure 8. (a) Wind stress vectors used in the mixed layer slab model (Pollard & Millard, 1970). (b) Comparison between modeled and observed near-inertial velocity magnitudes. (c) Energy flux from the wind to near-inertial velocity. (d) Time integral of the energy flux in (c).

can be compared to observed flows. Assuming changes in the MLD to be negligible compared to wind stress changes, the equation for Z_I is (D'Asaro, 1985):

$$\frac{dZ_I}{dt} + \omega Z_I = -\frac{1}{\omega H}\frac{dT}{dt}. \tag{10}$$

The model was ran between Days 30 and 55 by integrating Equation 10 using $H = 20$ m, the observed wind stress magnitudes (Figure 8a), and the near-inertial velocity at the start of Day 30 as the initial condition. Although impulse wind stresses can force near-inertial velocities, in the Southern (Northern) Hemisphere, near-inertial velocities best respond to anticlockwise- (clockwise-) rotating wind stresses (D'Asaro, 1985). Anticlockwise-rotating wind stress vectors are observed during the strong wind events around Days 39, 44, 47, 48, and 50, and these produce correspondingly strong modeled near-inertial velocities with magnitudes of ~0.05–0.09 m s^{-1} (Figure 8b). The modeled near-inertial velocity magnitudes exhibit a significant correlation of $R = 0.28$ ($p = 0.01$) with observations. The modeled velocities in response to the strong wind events are generally overestimated after Day ~39. This could be a consequence of the observed mixed layer deepening (and likely associated near-inertial flow dampening) that is not captured by the model, which

relies on a constant mixed layer depth; the mixed layer deepened from ~15 m on Day 37 to ~30 m on Day 43. The model's inability to characterize rapid mixed layer deepening has been documented previously and is thought to cause biases in near-inertial velocities of up to a factor of 4 (Plueddemann & Farrar, 2006).

An approximation of the energy flux into inertial motions from the winds can be given by Alford (2003):

$$\Pi = \Re[\rho Z_I T^*], \tag{11}$$

where $\Re$ extracts the real part of the solution and * indicates the complex conjugate. Although this equation neglects the term of order r_d/f (Alford, 2003), it does have utility in estimating the likely energy transfers. The energy flux can be positive or negative, with winds either accelerating or decelerating the inertial velocities, respectively (Figure 8c). Negative fluxes occur when the winds do work against the surface currents, causing increased shear and promoting the dissipation of turbulent kinetic energy (D'Asaro, 1985). The modeled energy fluxes typically have the same sign as the observations, but often produce larger velocities during strong wind events. This is seen more clearly in a time integral of the energy flux (Figure 8d), which shows a significant divergence between modeled and observed values after the first large wind event on Day 39. Although this exemplifies the model caveats mentioned above, Figures 8c and 8d also show large positive and negative fluxes on Days 39, 44, 47, and 50. This likely means that those wind events are particularly significant in affecting thermocline dissipation.

3.2.3. Deep Turbulent Dissipation

A common mechanism proposed for elevated mixing over topographic ridges similar to that found at the mouth of Ryder Bay is the breaking of internal tides (e.g., Polzin et al., 1997). The UTide Matlab package (Codiga, 2011) is used to carry out a harmonic analysis of the ADCP mooring data, to assess the magnitude and phase of internal tides in Ryder Bay. The harmonic analysis reveals the K_1 (32% of the total tidal amplitude) and O_1 (14%) tides to be the dominant barotropic constituents. These are reconstructed and compared to the measured barotropic u' (Figures 9a and 9c) and v' (Figures 9b and 9d) signals. Overall, mean absolute velocities of 1 cm s^{-1} were observed in both the u' and v' barotropic signals, with maximum total velocities of ~5–6 cm s^{-1}. The u' tidal component is comparatively weak throughout the deployment, with maximum amplitudes of 0.4 cm s^{-1}. The v' tidal velocities are larger (~1 cm s^{-1}) and can be of similar amplitude as the overall flow during periods of the spring tidal maximum (e.g., between Days 36 and 44; Figure 9d). Nevertheless, similarly large sub-inertial flows (~4−5 cm s^{-1}) occur, both at the spring maximum (e.g., Days 25 and 40) and neap minimum (e.g., Days 44 and 50). This implies that other processes are also likely to be important for setting the dynamics of the flow over the ridge. This is also supported by a substantial reduction in the larger velocities with the presence of fast-ice (Figures 9a and 9b), suggesting a significant influence of surface processes on the deep sub-inertial velocity field.

Hourly mean dissipation rates below 200 m and between 1.3 and 5.5 km along the A-B Transect (i.e., over the ridge) are compared with the observed K_1O_1 tidal barotropic velocities (Figures 9c and 9d). No significant correlation is found between the u' and v' barotropic K_1O_1 tidal components and the mean dissipation over the ridge, despite the occurrence of low-frequency features like the 2–3 cm s^{-1} negative u' velocities around Day 45. During certain periods, peaks in dissipation rate do appear to coincide with peaks in the reconstructed v' tidal velocities (e.g., on Days 42 and 43); however, there are also clear instances when this is not the case (e.g., on Day 49). Therefore, while the tides may play a role in governing the cross-shore flow and could be a source of elevated dissipation over the ridge, other processes are also likely to be at least as significant.

Various features of the hydrographic and dissipation rate data suggest that the flow over the ridge may be subject to hydraulic control, which could be implicated in the enhanced near-bottom dissipation over the ridge. The first piece of evidence for this is the elevated dissipation in Figure 4a at ~340 m depth, where the 27.74 kg m^{-3} isopycnal has the steepest slope. Such an arrangement, including pinching of the 27.73–27.74 kg m^{-3} isopycnal structure over the ridge, and deepening in its lee, is strongly reminiscent of flow that is controlled hydraulically (Farmer & Dungan Smith, 1980). Consequently, we apply layered hydraulic control theory to explore whether hydraulic physics may be applicable to our observations (i.e., whether such a control may be a plausible explanation for the observed dissipation over the ridge in Ryder Bay). We recognize that there are large limitations to using the theory in this way; however, since we lack upstream

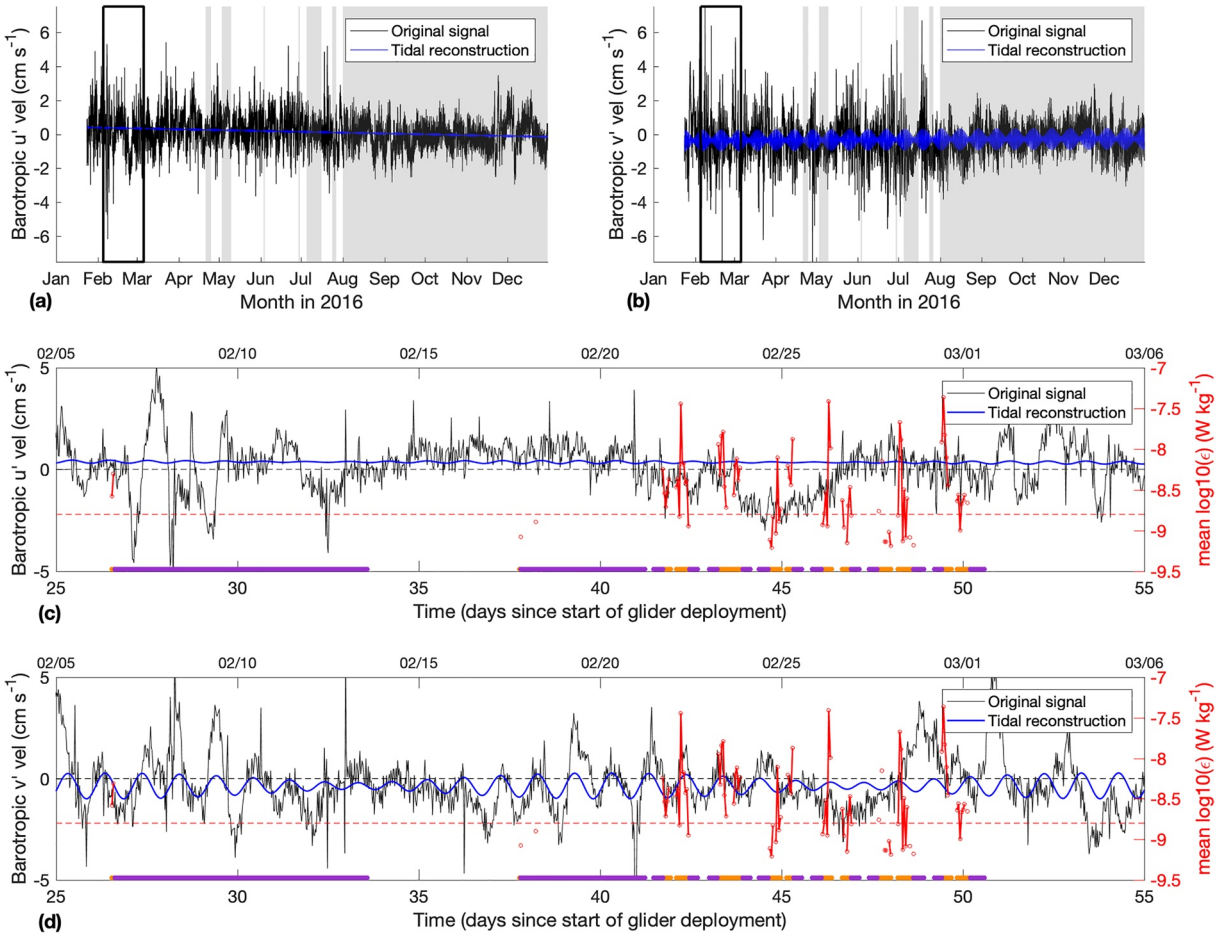

Figure 9. (a) Comparison of the barotropic u' velocity with corresponding reconstructed K_1/O_1 tidal component for 2016. The black outline and gray regions highlight Days 25–55 and periods with fast-ice present, respectively. (b) As (a), but for v' velocity. (c) u' velocity between Days 25 and 55 of the glider deployment. Overlain are hourly mean dissipation rates above the ridge (below 200 m and between 1.3 and 5.3 km along the A-B Transect). Horizontal dashed lines are corresponding overall mean values between Days 20 and 100 (the first ice-free period). (d) Same as (c) but for v' velocity.

velocity measurements, we opt for conducting a sensitivity analysis using the simplest theory available containing stratification. We therefore consider the composite Froude number, G^2, for a two-layer flow with a free surface (Armi, 1986):

$$G^2 = F_1^2 + F_2^2 - \frac{\rho_2 - \rho_1}{\rho_2} F_1^2 F_2^2, \tag{12}$$

where

$$F = \frac{u_{1,2}^2}{g' y_{1,2}} \text{ and } g' = g\frac{\rho_2 - \rho_1}{\rho_2}.$$

$u_{1,2}$ (m s^{-1}) and $y_{1,2}$ (m) are the upper (1) and lower (2) layer velocities and thicknesses, respectively, and g' is the reduced gravity. This theory assumes frictionless, nonrotational, incompressible, and hydrostatic flow with layers of uniform density and velocity (Armi, 1986). Additionally, time-dependent, mixing, and stable stratification effects are ignored (Hogg & Killworth, 2004).

In a system that is controlled hydraulically, flow transitions from low velocities in a sub-critical regime ($G^2 < 1$) upstream of a topographic ridge, to fast velocities in a supercritical ($G^2 > 1$) regime above and in the lee of the ridge, before transitioning back to sub-critical flow further downstream (Armi, 1986). The point

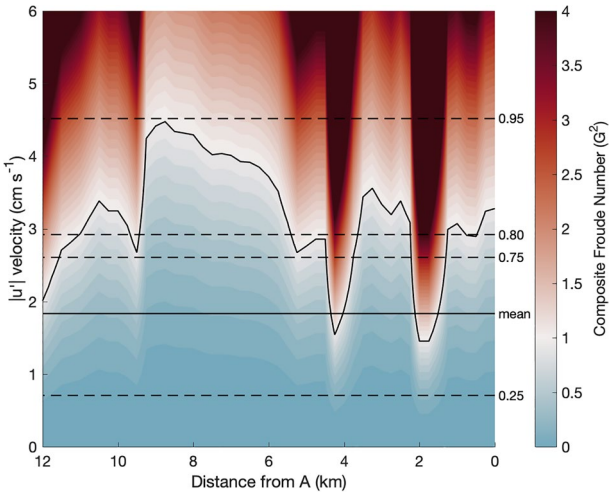

Figure 10. Composite Froude number sensitivity analysis, using layer thicknesses from Transect 4 (Figure 4a). The black contour depicts 1, the critical Froude number. The mean absolute velocity between 245 and 308 m and days 20–100 is overlain, along with the 25, 75, 80 and 95th percentiles. Contours are in 0.1 increments from 0 to 4.

of criticality ($G^2 = 1$) marks the transition between sub to supercritical flow, and can move with respect to the ridge due to changes in flow speed, where a faster flow tends to move the point of criticality upstream (Farmer & Denton, 1985). In a supercritical flow over a ridge, dissipation rates can reach several orders of magnitude higher than background values, due to increased ridge-flow interactions (Gregg & Klymak, 2014). At the transition between super to sub-critical flow, the decrease in flow speed can cause the formation of a hydraulic jump and the release of a large amount of energy through elevated dissipation (Farmer & Denton, 1985).

The downstream ADCP mooring within Ryder Bay provides a range of likely velocities that can be used in the composite Froude number sensitivity analysis. Over 95% of the observed $|u'|$ values between 250 and 300 m fall between 0 and 6 cm s^{-1}, with mean, 25th and 75th percentile velocities of 1.8, 0.7, and 2.6 cm s^{-1}, respectively (horizontal lines, Figure 10; exact ADCP depth bins are quoted in the caption). This depth range spans the region over the ridge where the 27.73–27.74 kg m^{-3} isopycnals commonly pinch together in Transect 4 (Figure 4a). Only velocities between Days 20 and 100 are considered, as this is the ice-free period over which the same processes are thought to occur. Consequently, the sensitivity analysis applies constant velocities between 0 and 6 cm s^{-1} across the length of the transect. ADCP velocities below 250 m depth are relatively constant, so here $u_1 = u_2$; note, though, that setting $u_2 > u_1$, as may be expected over the ridge, only acts to increase the composite Froude numbers (not shown).

The composite Froude number analysis requires assignment of a constant density to each of the two layers within the equation. Since the data is continuous, there is no rigorous way to choose these layers, so we selected isopycnals that are the most reminiscent of hydraulic control, pinching over the ridge and steeply sloping in its lee, and that still had significant layer thicknesses (>50 m) at the mooring location in Transect 4 (Figure 4a). Consequently, the 27.735 and 27.74 kg m^{-3} isopycnals are selected as the upper bounds for each of the two layers, and the layer thicknesses are calculated from each glider transect density field. The layer thicknesses are then used in conjunction with the velocities mentioned above to generate G^2 values along the A-B Transect for each glider transect. Figure 10 shows the G^2 values produced for Transect 4. Composite Froude numbers peak at 1.75 and 4.25 km along the section, with values of 1.5 and 4 generated at mean velocities. At these velocities, downstream Froude numbers are less than 1 (e.g., between 5.75 and 9.25 km). This indicates a transition from super to sub-critical flow, and suggests that the flow over the ridge into Ryder Bay could be controlled hydraulically.

We reiterate that this analysis is limited; however, the lack of upstream velocities means that the simplest layered theory is the best available option. To assess the sensitivity of this analysis to layer choices, G^2 was recalculated while keeping all inputs the same, but using the 27.72 and 27.74 kg m^{-3} isopycnals, thereby increasing the density difference between the two layers (over the ridge in Transect 4, this is equivalent to a 40 m increase in vertical distance between the two isopycnals). The 27.72 kg m^{-3} isopycnal was selected because it is close to the lightest density thought to be influenced by the hydraulic control (judging by the decrease in depth at 6.5 km; Figure 4a). Composite Froude numbers are greatly reduced across the A-B Transect, and larger velocities are required to reach criticality (not shown). That said, G^2 values > 1 are still found over the ridge (at 1.75 and 4.25 km) and are sub-critical downstream, at velocities marginally greater than the 80th percentile velocity of 2.9 cm s^{-1}. Under hydraulic conditions, velocities increase where the density layers thin and pinch together. Consequently, velocities greater than the mean from the downstream mooring are perhaps actually expected.

The Froude number sensitivity analysis using the 27.735 and 27.74 kg m^{-3} isopycnals revealed that 7 out of the 11 complete glider transects met the following three criteria, used to suggest the presence of a hydraulic control over the ridge: (i) elevated dissipation; (ii) $G^2 > 1$ at the mean velocity; and (iii) pinching and steeply sloping isopycnals. This demonstrates that the deep elevated dissipation is a consistent feature. The location

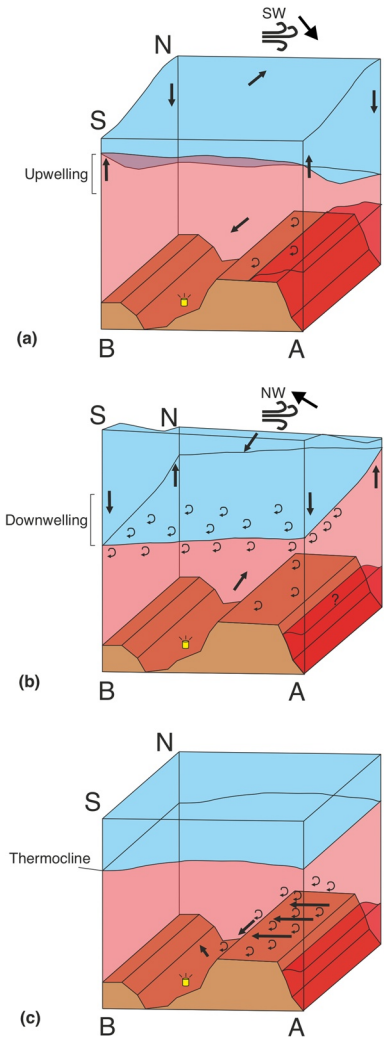

Figure 11. Three-stage schematic showing the processes proposed to explain the observed dissipation patterns within Ryder Bay. Mechanisms are in the order discussed in the text. Straight arrows show flow direction; curly arrows represent enhanced dissipation; yellow symbol shows the ADCP mooring. (a) South-westward winds drive flow toward the bay's northern boundary above the pycnocline, and toward the southern boundary at depth, leading to upwelling on the southern side of Ryder Bay, as recorded by the ADCP mooring. (b) North-westward winds have the opposite effect, driving southward flow above the pycnocline and northward flow at depth, leading to downwelling on the southern side of Ryder Bay. Following downwelling, winds rotate anticlockwise and generate near-inertial shear and dissipation at the base of the thermocline. (c) Hydraulic control causes faster flow over the ridge leading to enhanced dissipation.

of the pinching and steeply sloping isopycnals varies between these transects, and the location of the elevated dissipation changes accordingly. This likely represents a shift in the position of flow criticality (due to variable flow speeds), moving the region of supercritical flow and elevated dissipation rates accordingly. Taken alongside the scant evidence for internal tidal control of dissipation at this ridge, we suggest that hydraulic control is likely to be a key mechanism in determining the observed deep dissipation. Its impact on vertical heat fluxes is discussed in greater detail in Section 4.

4. Summary and Discussion

This study has presented some of the first direct estimates of the dissipation of turbulent kinetic energy in west Antarctica. Mean ϵ values above the topographic ridge separating Ryder Bay from LF are generally elevated compared with those observed within the basin. However, the 12 glider transects reveal significant temporal variability in Ryder Bay's hydrography and dissipation rates. Synthesizing the analysis above, the proposed mechanisms for this observed temporal variability are discussed (Figure 11) next, and their likely contribution to Ryder Bay's heat budget is assessed.

4.1. Proposed Mechanisms Regulating Hydrography and Dissipation

4.1.1. Thermocline Depth—Wind-Induced Coastal Upwelling/Downwelling

The observed shoaling followed by a sudden deepening of the thermocline between Transects 10 and 12 (Days 47 and 49, respectively; Figures 4b and 4c) is interpreted here as coastal upwelling (Figures 11a) followed by downwelling (Figures 11b) on Ryder Bay's southern boundary. This occurred in response to south-westward and north-westward wind events centered around Days 39 and 44. This interpretation is supported by the mixed layer slab model, which predicts upper layer velocities that are conducive to Ekman upwelling and downwelling in response to the Days 39 and 44 wind events (Appendix A).

Wind stress magnitude and direction are seemingly important for the spin-up of this bay-scale circulation, with both events coinciding with strong winds of >25 m s^{-1} over a period of ~3 days, and low wind direction variance (Figure 5b). The Days 39 and 44 wind events were therefore able to drive sustained surface Ekman layer flow toward Ryder Bay's northern and southern boundaries, respectively, and acted over a sufficiently long time to initiate a deep opposing flow at depth (through mass conservation). This lower-layer response occurred ~3 days after the start and end of the respective wind events, in line with previous estimates of wind-induced upwelling time scales of 2–7 days within Ryder Bay (Wallace et al., 2008). The longer lower-layer response to the Day 44 wind event (i.e., from the end of the event rather than the start) could be associated with the stalling and reversal of upwelling on the bay's southern boundary. This is reflected in the mean 200 m temperature data; the temperature steadily increases, stabilizes, and then rapidly decreases on Day 48 (Figure 6c). The rate of downwelling on Day 48 may have been invigorated by the south-westward winds on Day 47 (Figure 5a) which, due to their strength and low variance, must have induced large upper-layer flow with a similar alignment to the winds to penetrate deeper into the water column (not shown). Although strong south-westward winds similar to those of the Day 39

wind event are observed after Day 46 (Figure 6a), the lack of an upwelling signal may relate to the large variability in flow direction, with most days hosting elevated circular variance from Day 50 onward (Figure 5b).

4.1.2. Thermocline Dissipation—Wind-Generated Near-Inertial Shear

Dissipation rates within the thermocline (105−205 m) are believed to be controlled by wind-induced near-inertial shear (Figures 7 and 11b). In particular, the basin-wide dissipation event on Day 49 (Transect 12; Figure 4c) is ascribed to strong wind stress on Day 47 (red arrow; Figure 7a). This interpretation is supported by the statistically significant correlations between the 4-day low-pass filtered wind stress and near-inertial thermocline shear ($R = 0.92$, $p \ll 0.001$; after a 1.7-day lag-adjustment), and between the thermocline shear and dissipation before Day 41.25 ($R = 0.38$, $p = 0.01$). Although the correlation after Day 43.5 is only significant to the 10% level ($R = 0.24$, $p = 0.06$), we continue to suggest that wind-driven near-inertial shear primarily controls thermocline dissipation, since other possible mechanisms, such as CTWs and basin-scale wave modes, do not appear to be important within Ryder Bay (not shown). Additionally, the 1.7-day lag is similar to that documented by Forryan et al. (2015), and supports their proposition that undocumented frontal-scale processes must efficiently inject near-inertial shear into the ocean interior. The interpretation is also supported by the mixed layer slab model, which predicted high near-inertial velocities and negative energy fluxes (promoting shear and dissipation) in response to strong wind forcing (D'Asaro, 1985).

Differences between near-inertial shear and dissipation at the thermocline may be due to both spatial variability and the presence of super-inertial shear. Even within the 105–205 m layer, there is still a spatial pattern in the dissipation, with elevated dissipation over the ridge compared to above the basin. Differentiating between this spatial pattern and the temporal control associated with wind-induced shear is not possible with the data available in this study. This could explain the high dissipation between Days 41.25 and 43.50, and the marginal statistical insignificance (at the 5% level) for the correlation after Day 43.5. Additionally, storms can also generate super-inertial shear and dissipation, both via the wind working to directly excite super-inertial waves, and via the nonlinear cascade of energy from near- to super-inertial frequencies (Jing et al., 2015). Super-inertial energy could therefore be responsible for other periods of elevated dissipation concurrent with low near-inertial shear away from the ridge; for example, the elevated dissipation spike at the start of Day 49 (Figure 7c). This would suggest that different frequency bands are important at different times.

4.1.3. Deep Dissipation—Hydraulic Structure

The elevated dissipation observed ≤200 m above the ridge is interpreted here as being, at least in part, controlled hydraulically (Figures 11c). This is primarily due to the elevated dissipation consistently occurring at the location of the steepest isopycnals, despite their position relative to the ridge varying with time. This is characteristic of a hydraulic structure translated spatially by changing flow speeds. Although this study lacks upstream velocity measurements, and therefore the calculation can only be exploratory, the possibility of hydraulic control is supported by a composite Froude number sensitivity analysis, which exhibits the required transition from super to sub-critical flow moving over the ridge into the basin (Figure 10). This occurs over a range of possible velocities, including those similar to the overall mean (1.8 cm s^{-1}), the Day 45 mean barotropic u' velocity (~2 cm s^{-1}), and the 80th percentile (2.9 cm s^{-1}). A transition from super to sub-critical flow is still generated when using larger density differences in the calculation, although higher velocities are required to reach criticality (not shown). While internal tides commonly form hydraulic structure and cause elevated dissipation over topography (e.g., Gregg & Klymak, 2014; Klymak & Gregg, 2004), reconstructed K_1O_1 tidal velocities into and out of the bay are negligible (alongshore, u'; Figure 9c), in line with previous observations of weak tides in Ryder Bay (e.g., Brearley et al., 2017; Wallace et al., 2008). This suggests that internal tides are not responsible for the formation of a hydraulic structure over the ridge. Cross-shore K_1O_1 velocities are larger and could have a role in controlling dissipation, particularly during the spring/neap maximum when they can dominate barotropic flow (Figure 9c). However, the orientation of these tides (down the length of the ridge) is not conducive to a hydraulic control situation, and elevated dissipation is observed throughout the deployment, at different stages of the spring/neap tidal cycle. This suggests that other processes are likely at play. For example, the role of wind-driven Ekman upwelling/downwelling in driving the deep dissipation is unknown, but could cause elevated dissipation through increased ridge-flow interaction at times in which the deep inflow to the bay is enhanced. Additionally, the deep flow toward Ryder Bay's southern boundary could induce bottom Ekman flow into the bay, potentially leading to

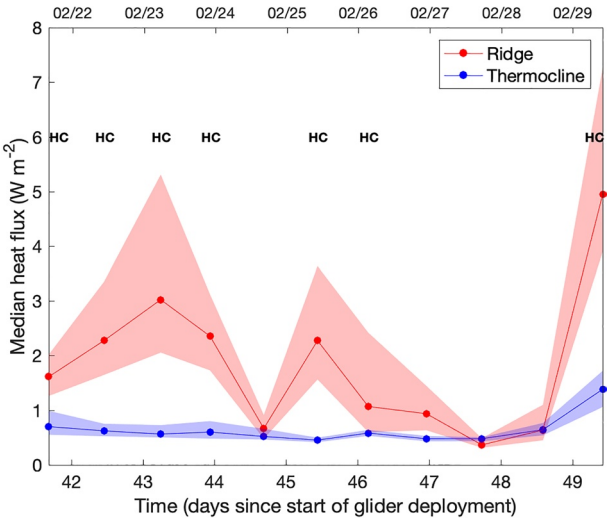

Figure 12. Comparison of median vertical heat fluxes for Transects 2–12 (the complete transects). Deep heat fluxes were calculated at ≤200 m and between 1.3 and 5.5 km. Thermocline heat fluxes are calculated over 105–200 m depth, across the full length of the section. Shaded regions show 90% bootstrapped errors. Transects that meet the three criteria resembling a hydraulic control (HC) scenario, are indicated.

a hydraulic structure and elevated dissipation. Indeed, the lower-frequency variability in the barotropic velocities decreases with the presence of sea ice, suggesting that atmospheric forcing is (at least in part) important. The low-frequency variability could be related to wind-driven changes on the continental slope, either linked to local winds (Dotto et al., 2019) or large-scale wind forcing (Naveira Garabato et al., 2019).

4.2. Two-Stage Upward Heat Flux and Wider Implications

The contributions of the proposed mechanisms to the heat budget are explored by calculating the upward heat flux (Q), associated with the deep and thermocline dissipation in each of the complete Transects (2–12; Figure 12) using

$$Q = \rho_0 C_p \kappa_p \frac{\partial \theta}{\partial z}, \tag{13}$$

where positive Q is upwards, ρ_0 is the reference density (1.025×10^3 kg m^{-3}), C_p is the specific heat capacity at constant pressure 4,000 J kg^{-1} °C^{-1}, and κ_ρ is the diapycnal diffusivity. Overall, median heat fluxes over the ridge are ~3 times greater than in the thermocline. Sloping isopycnals and elevated dissipation reminiscent of a hydraulic control scenario are observed in 7 out of the 11 transects (~60%); in these cases, the mean median ridge heat flux is 2.4 W m^{-2}, ~4 times greater than thermocline fluxes and transects without such features (~0.6 W m^{-2}). These heat fluxes are of a similar magnitude to previous estimates in the WAP shelf (Brearley et al., 2017; Howard et al., 2004).

The disparity between the ridge and thermocline heat flux magnitudes suggests either an accumulation of heat at the base of the thermocline above the ridge, or perhaps more likely, that the heat spreads laterally at this depth, with spatially homogeneous mixing across the thermocline's base at a lower rate but over a larger area. Given the available data, we are unable to quantify these lateral heat fluxes, so here we settle for a crude, one-dimensional order-of-magnitude calculation. If the ridge heat fluxes associated with a hydraulic structure occur in 60% of the transects (which take approximately a day to complete), over the 6-month spring/summer period (when the proposed mechanisms might be expected) there would be a ~22 MJ m^{-2} upward heat flux to the base of the thermocline. Over an unknown area, this heat would then mix across the thermocline into the overlying waters at a slower rate of 0.6 W m^{-2} per day (~9 MJ m^{-2} over 6 months).

Basin-wide thermocline dissipation events, generated by wind-induced near-inertial shear, support periods of intensified mixing. Figure 12 shows that the median thermocline heat flux on Day 49, the day of the basin-wide thermocline dissipation (Figure 4c), is two times as large (1.3 W m^{-2}) as typical values (~0.6 W m^{-2}). This suggests that strong winds events like that observed on Day 47 (red arrow; Figure 7a) can cause a widespread release of heat across the thermocline and into the overlying cooler waters. Day 49, ridge heat fluxes are also elevated; however, given the available data, it is not possible to attribute this to a single mechanism. Additionally, the Ekman coastal upwelling/downwelling processes discussed here are important because, by altering the depth of the thermocline, they can alter the amount of heat readily available for wind- and ridge-induced vertical mixing.

This study documents a two-stage upward heat flux within Ryder Bay: a persistent flux over the ridge, likely associated with a hydraulic control scenario; and an intermittent, usually weaker cross-thermocline flux linked to strong wind forcing events that release heat into the overlying winter mixed layer. Waters in this layer can come into direct contact with the atmosphere (during winter, when the mixed layer is deeper), ice shelves at similar depths, and marine-terminating glaciers (Sheldon Glacier's grounding line is thought to be at ~200 m. This result, in conjunction with the comparable magnitude of our diagnosed heat fluxes and those commonly associated with ice shelf melting (8 W m^{-2}; Jenkins & Jacobs, 2008), highlights the potential importance of a two-stage upwards heat flux triggered by ridge-flow interaction and wind forcing for

the WAP heat budget. CDW enters Ryder Bay having first been advected through MT and LF, both of which contain many ridges where vertical mixing could occur (Venables et al., 2017). Consequently, the ridges are likely to be hotspots for bringing heat to the base of the thermocline. Future fast-ice trends are uncertain (Stammerjohn et al., 2008), but a decrease in ice cover and increasing storm activity associated with a positive Southern Annular Mode index (Lefebvre et al., 2004) would arguably allow more storms to penetrate deeper into the water column over longer periods (Brearley et al., 2017; Venables & Meredith, 2014). This could result in reduced stratification, greater thermocline heat fluxes, and possibly more heat available to melt ice. Ryder Bay is analogous to many other embayments off the WAP that have similar ridges, which suggests that similar processes may also be operating in other locations across the WAP shelf.

Appendix A: Modeled/Observed Ekman Velocities

Observed Ekman velocities were calculated by subtracting the observed near-inertial (0.9–1.9*f*) velocities from the original signal. The modeled Ekman velocities agree with observations throughout, including the days thought to be important for the suggested Ekman upwelling/downwelling (Figure A1).

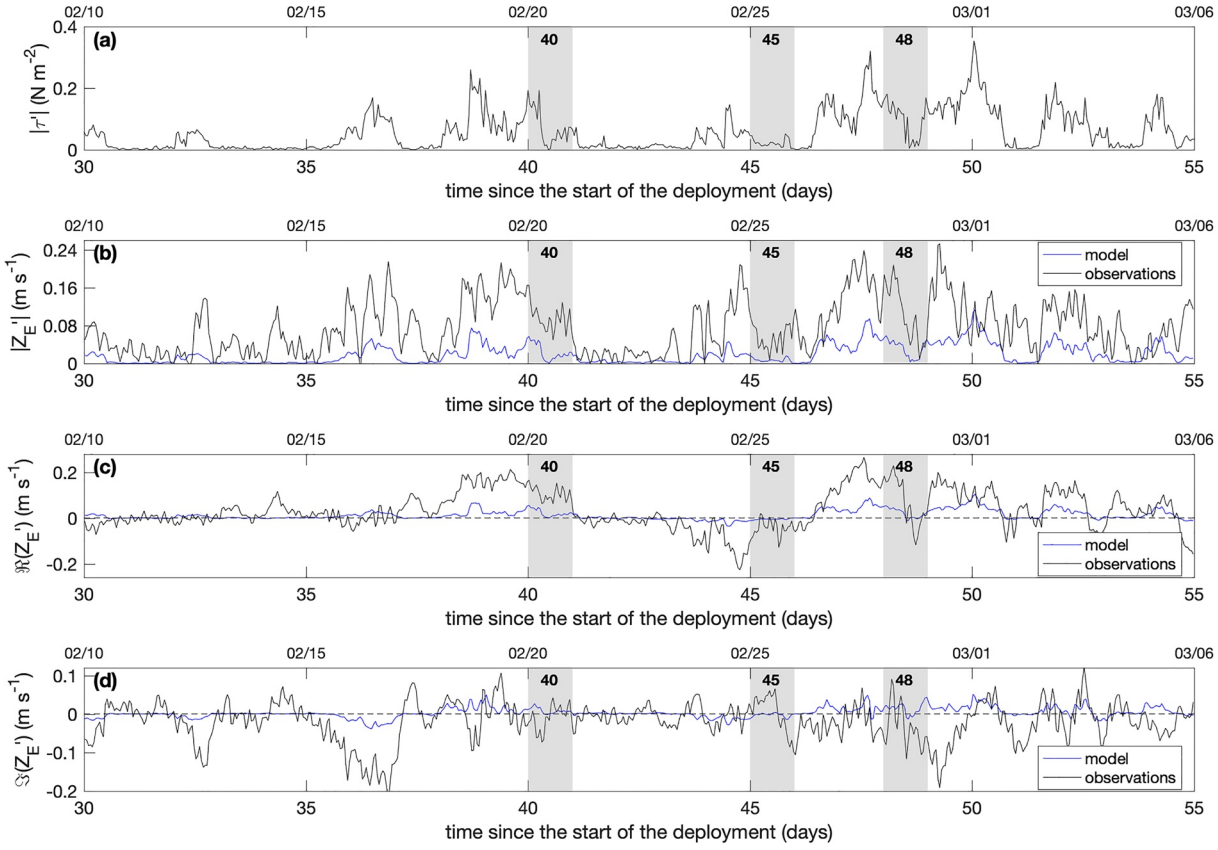

Figure A1. (a) Wind stress magnitude used in the mixed layer slab model (Pollard & Millard, 1970). (b) Comparison between modeled and observed Ekman velocity magnitudes. The real (c) and imaginary (d) velocity components are positive in the u' and v' directions, respectively. Gray columns show the following days of interest: 40, 45, and 48.

Data Availability Statement

Rothera meteorological data can be found at https://legacy.bas.ac.uk/cgi-bin/metdb-form-1.pl?table\text{_}prefix=U\text{_}WMC,U\text{_}MET&acct=u\text{_}met&pass=weather. RaTS data can be found at https://www.bodc.ac.uk/resources/inventories/edmed/report/4278/. Processed glider and ADCP data are available through https://doi.org/10/fx2f and https://doi.org/10/fsjg, respectively.

Acknowledgments
The authors would like to thank those involved in deploying and recovering the glider and mooring used in this study, the Marine Assistants who collect the Rothera Time Series (RaTS), and Laura Gerrish from the MAGIC Department at the British Antarctic Survey, who created Figure 1a. The authors would also like to thank Dr. Lucas Merckelbach and Prof. Mark Inall for their help setting up the hydrodynamic flight model and analysis of basin-scale wave modes and CTWs, respectively. The authors also thank Dr. Borja Aguiar-González and an anonymous reviewer for providing useful feedback that significantly improved the manuscript. This study was supported by the Natural Environmental Research Council (Grant numbers NE/N012070/1 [Ryan M. Scott], NE/R016038/1 [J. Alexander Brearley, Hugh J. Venables, and Michael P. Meredith], and NE/L011166/1 [J. Alexander Brearley]. RaTS is a component of the BAS Polar Oceans program, funded by NERC. Alberto C. Naveira Garabato acknowledges the support of the Royal Society and the Wolfson Foundation.

References

Alford, M. H. (2001). Internal swell generation: The spatial distribution of energy flux from the wind to mixed layer near-inertial motions. *The Journal of Physical Oceanography*, *31*(8), 2359–2368. https://doi.org/10.1175/1520-0485(2001)031<2359:isgtsd>2.0.co;2

Alford, M. H. (2003). Improved global maps and 54-year history of wind-work on ocean inertial motions. *Geophysical Research Letters*, *30*(8). https://doi.org/10.1029/2002gl016614

Allen, J. S. (1975). Coastal trapped waves in a stratified ocean. *Journal of Physical Oceanography*, *5*(2), 300–325. https://doi.org/10.1175/1520-0485(1975)005<0300:ctwias>2.0.co;2

Armi, L. (1986). The hydraulics of two flowing layers with different densities. *Journal of Fluid Mechanics*, *163*, 27–58. https://doi.org/10.1017/s0022112086002197

Arneborg, L., & Liljebladh, B. (2001). The internal seiches in Gullmar Fjord. Part II: Contribution to basin water mixing. *Journal of Physical Oceanography*, *31*(9), 2567–2574. https://doi.org/10.1175/1520-0485(2001)031<2567:tisigf>2.0.co;2

Arneborg, L., Wåhlin, A. K., Björk, G., Liljebladh, B., & Orsi, A. H. (2012). Persistent inflow of warm water onto the central Amundsen shelf. *Nature Geoscience*, *5*(12), 876. https://doi.org/10.1038/ngeo1644

Berens, P. (2009). CircStat: A MATLAB toolbox for circular statistics. *The Journal of Statistical Software*, *31*(10), 1–21. https://doi.org/10.18637/jss.v031.i10

Brearley, J. A., Meredith, M. P., Naveira Garabato, A. C., Venables, H. J., & Inall, M. E. (2017). Controls on turbulent mixing on the West Antarctic Peninsula shelf. *Deep Sea Research Part II: Topical Studies in Oceanography*, *139*, 18–30. https://doi.org/10.1016/j.dsr2.2017.02.011

Chereskin, T. K., & Roemmich, D. (1991). A comparison of measured and wind-derived Ekman transport at 11°N in the Atlantic Ocean. *Journal of Physical Oceanography*, *21*(6), 869–878. https://doi.org/10.1175/1520-0485(1991)021<0869:acomaw>2.0.co;2

Codiga, D. L. (2011). *Unified tidal analysis and prediction using the UTide Matlab functions*. Graduate School of Oceanography, University of Rhode Island.

Cook, A. J., Fox, A. J., Vaughan, D. G., & Ferrigno, J. G. (2005). Retreating glacier fronts on the Antarctic Peninsula over the past half-century. *Science*, *308*(5721), 541–544. https://doi.org/10.1126/science.1104235

Cook, A. J., Holland, P. R., Meredith, M. P., Murray, T., Luckman, A., & Vaughan, D. G. (2016). Ocean forcing of glacier retreat in the Western Antarctic Peninsula. *Science*, *353*(6296), 283–286. https://doi.org/10.1126/science.aae0017

D'Asaro, E. A. (1985). The energy flux from the wind to near-inertial motions in the surface mixed layer. *Journal of Physical Oceanography*, *15*(8), 1043–1059.

Dotto, T. S., Naveira Garabato, A. C., Bacon, S., Holland, P. R., Kimura, S., Firing, Y. L., et al. (2019). Wind-driven processes controlling oceanic heat delivery to the Amundsen Sea, Antarctica. *Journal of Physical Oceanography*, *49*(11), 2829–2849. https://doi.org/10.1175/JPO-D-19-0064.1

Dupont, T. K., & Alley, R. B. (2005). Assessment of the importance of ice-shelf buttressing to ice-sheet flow. *Geophysical Research Letters*, *32*(4). https://doi.org/10.1029/2004gl022024

Farmer, D. M., & Denton, R. A. (1985). Hydraulic control of flow over the sill in observatory inlet. *Journal of Geophysical Research*, *90*(C5), 9051–9068. https://doi.org/10.1029/JC090iC05p09051

Farmer, D. M., & Dungan Smith, J. (1980). Tidal interaction of stratified flow with a sill in Knight Inlet. *Deep Sea Research A. Oceanographic Research Papers*, *27*(3), 239–254. https://doi.org/10.1016/0198-0149(80)90015-1

Fiedler, P. C. (2010). Comparison of objective descriptions of the thermocline. *Limnology and Oceanography: Methods*, *8*(6), 313–325. https://doi.org/10.4319/lom.2010.8.313

Forryan, A., Naveira Garabato, A. C., Polzin, K. L., & Waterman, S. (2015). Rapid injection of near-inertial shear into the stratified upper ocean at an Antarctic Circumpolar Current front. *Geophysical Research Letters*, *42*(9), 3431–3441. https://doi.org/10.1002/2015gl063494

Fraser, N. J., Inall, M. E., Magaldi, M. G., Haine, T. W. N., & Jones, S. C. (2018). Wintertime Fjord-shelf interaction and ice sheet melting in Southeast Greenland. *Journal of Geophysical Research: Oceans*, *123*(12), 9156–9177. https://doi.org/10.1029/2018jc014435

Fremand, A. (2020). *Gridded bathymetric compilation of Ryder Bay from raw and processed multibeam echosounder data collected by the RRS James Clark Ross*. (2001–2016) [data set]. Retrieved from https://doi.org/10.5285/0F4D7D85-1E38-4E0E-80AF-1FCD85267FFC

Goodman, L., Levine, E. R., & Lueck, R. G. (2006). On measuring the terms of the turbulent kinetic energy budget from an AUV. *Journal of Atmospheric and Oceanic Technology*, *23*(7), 977–990. https://doi.org/10.1175/jtech1889.1

Gregg, M. C., & Klymak, J. M. (2014). Mode-2 hydraulic control of flow over a small ridge on a continental shelf. *Journal of Geophysical Research: Oceans*, *119*(11), 8093–8108. https://doi.org/10.1002/2014jc010043

Hogg, A. M., & Killworth, P. D. (2004). Continuously stratified exchange flow through a contraction in a channel. *Journal of Fluid Mechanics*, *499*, 257–276. https://doi.org/10.1017/S0022112003007171

Howard, S. L., Hyatt, J., & Padman, L. (2004). Mixing in the pycnocline over the western Antarctic Peninsula shelf during Southern Ocean GLOBEC. *Deep Sea Research Part II: Topical Studies in Oceanography*, *51*(17–19), 1965–1979. https://doi.org/10.1016/j.dsr2.2004.08.002

Huppert, H. E., & Turner, J. S. (1981). Double-diffusive convection. *Journal of Fluid Mechanics*, *106*, 299–329. https://doi.org/10.1017/s0022112081001614

Huss, M., & Farinotti, D. (2014). A high-resolution bedrock map for the Antarctic Peninsula. *The Cryosphere*, *8*(4), 1261–1273. https://doi.org/10.5194/tc-8-1261-2014

Hyatt, J., Beardsley, R. C., & Owens, W. B. (2011). Characterization of sea ice cover, motion and dynamics in Marguerite Bay, Antarctic Peninsula. *Deep Sea Research Part II: Topical Studies in Oceanography*, *58*(13–16), 1553–1568. https://doi.org/10.1016/j.dsr2.2010.08.021

Inall, M. E., Murray, T., Cottier, F. R., Scharrer, K., Boyd, T. J., Heywood, K. J., & Bevan, S. L. (2014). Oceanic heat delivery via Kangerlussuaq Fjord to the south-east Greenland Ice Sheet. *Journal of Geophysical Research: Oceans*, *119*(2), 631–645. https://doi.org/10.1002/2013jc009295

Inall, M. E., Nilsen, F., Cottier, F. R., & Daae, R. (2015). Shelf/Fjord exchange driven by coastal-trapped waves in the Arctic. *Journal of Geophysical Research: Oceans*, *120*(12), 8283–8303. https://doi.org/10.1002/2015jc011277

Jacobs, S. S., Hellmer, H. H., & Jenkins, A. (1996). Antarctic ice sheet melting in the Southeast Pacific. *Geophysical Research Letters*, *23*(9), 957–960. https://doi.org/10.1029/96GL00723

Jenkins, A., & Jacobs, S. (2008). Circulation and melting beneath George VI Ice Shelf, Antarctica. *Journal of Geophysical Research*, *113*(C04013). https://doi.org/10.1029/2007JC004449

Jing, Z., Chang, P., DiMarco, S. F., & Wu, L. (2015). Role of near-inertial internal waves in subthermocline diapycnal mixing in the northern Gulf of Mexico. *Journal of Physical Oceanography*, *45*(12), 3137–3154. https://doi.org/10.1175/jpo-d-14-0227.1

Klinck, J. M., Hofmann, E. E., Beardsley, R. C., Salihoglu, B., & Howard, S. (2004). Water-mass properties and circulation on the west Antarctic Peninsula Continental Shelf in Austral Fall and Winter 2001. *Deep Sea Research Part II: Topical Studies in Oceanography*, *51*(17–19), 1925–1946. https://doi.org/10.1016/j.dsr2.2004.08.001

Klymak, J. M., & Gregg, M. C. (2004). Tidally generated turbulence over the knight inlet sill. *Journal of Physical Oceanography*, *34*(5), 1135–1151. https://doi.org/10.1175/1520-0485(2004)034<1135:tgtotk>2.0.co;2

Lefebvre, W., Goosse, H., Timmermann, R., & Fichefet, T. (2004). Influence of the Southern Annular Mode on the sea ice–ocean system. *Journal of Geophysical Research: Oceans*, *109*(C9). https://doi.org/10.1029/2004jc002403

Legg, S., & Klymak, J. (2008). Internal hydraulic jumps and overturning generated by tidal flow over a tall steep ridge. *Journal of Physical Oceanography*, *38*, 1949–1964. https://doi.org/10.1175/2008jpo3777.1

Livingstone, S. J., Cofaigh, C. Ó., Stokes, C. R., Hillenbrand, C.-D., Vieli, A., & Jamieson, S. S. R. (2013). Glacial geomorphology of Marguerite Bay Palaeo-ice stream, western Antarctic Peninsula. *Journal of Maps*, *9*(4), 558–572. https://doi.org/10.1080/17445647.2013.829411

Lueck, R. (2013). *Tn 028: Calculating the rate of dissipation of turbulent kinetic energy*. Rockland Scientific International Inc.

Lueck, R. (2016). *Tn 005: Converting shear-probe, thermistor and micro-conductivity signals into physical units*. Rockland Scientific International Inc.

Lueck, R. G., Wolk, F., & Yamazaki, H. (2002). Oceanic velocity microstructure measurements in the 20th century. *Journal of Oceanography*, *58*(1), 153–174. https://doi.org/10.1023/a:1015837020019

Martinson, D. G., & McKee, D. C. (2012). Transport of warm Upper Circumpolar Deep Water onto the western Antarctic Peninsula continental shelf. *Ocean Science*, *8*(4), 433. https://doi.org/10.5194/os-8-433-2012

Martinson, D. G., Stammerjohn, S. E., Iannuzzi, R. A., Smith, R. C., & Vernet, M. (2008). Western Antarctic Peninsula physical oceanography and spatio–temporal variability. *Deep Sea Research Part II: Topical Studies in Oceanography*, *55*(18–19), 1964–1987. https://doi.org/10.1016/j.dsr2.2008.04.038

Merckelbach, L., Berger, A., Krahmann, G., Dengler, M., & Carpenter, J. R. (2019). A dynamic flight model for Slocum gliders and implications for turbulence microstructure measurements. *Journal of Atmospheric and Oceanic Technology*, *36*(2), 281–296. https://journals.ametsoc.org/doi/abs/10.1175/JTECH-D-18-0168.1

Merckelbach, L., Smeed, D., & Griffiths, G. (2010). Vertical water velocities from underwater gliders. *Journal of Atmospheric and Oceanic Technology*, *27*(3), 547–563. https://doi.org/10.1175/2009jtecho710.1

Mickett, J. B., Serra, Y. L., Cronin, M. F., & Alford, M. H. (2010). Resonant forcing of mixed layer inertial motions by atmospheric easterly waves in the northeast tropical pacific. *Journal of Physical Oceanography*, *40*(2), 401–416. https://doi.org/10.1175/2009jpo4276.1

Mitchum, G. T., & Clarke, A. J. (1986). The frictional nearshore response to forcing by synoptic scale winds. *Journal of Physical Oceanography*, *16*(5), 934–946. https://doi.org/10.1175/1520-0485(1986)016⟨0934:TFNRTF⟩2.0.CO;2

Moffat, C., & Meredith, M. (2018). Shelf-ocean exchange and hydrography west of the Antarctic Peninsula: A review. *Philosophical Transactions of the Royal Society A: Mathematical, Physical & Engineering Sciences*, *376*(2122). https://doi.org/10.1098/rsta.2017.0164

Moffat, C., Owens, B., & Beardsley, R. C. (2009). On the characteristics of Circumpolar Deep Water intrusions to the west Antarctic Peninsula Continental Shelf. *Journal of Geophysical Research*, *114*(C5). https://doi.org/10.1029/2008jc004955

Muench, R. D., Fernando, H. J. S., & Stegen, G. R. (1990). Temperature and salinity staircases in the northwestern Weddell Sea. *Journal of Physical Oceanography*, *20*(2), 295–306. https://doi.org/10.1175/1520-0485(1990)020<0295:tassit>2.0.co;2

Nasmyth, P. W. (1970). *Oceanic turbulence (Unpublished doctoral dissertation)*. University of British Columbia.

Naveira Garabato, A. C., Dotto, T. S., Hooley, J., Bacon, S., Tsamados, M., Ridout, A., et al. (2019). Phased response of the subpolar southern ocean to changes in circumpolar winds. *Geophysical Research Letters*, *46*(11), 6024–6033. https://doi.org/10.1029/2019GL082850

Orsi, A. H., Whitworth, T., & Nowlin, W. D. (1995). On the meridional extent and fronts of the Antarctic Circumpolar Current. *Deep Sea Research I: Oceanographic Research Papers*, *42*(5), 641–673. https://doi.org/10.1016/0967-0637(95)00021-W

Osborn, T. R. (1980). Estimates of the local rate of vertical diffusion from dissipation measurements. *Journal of Physical Oceanography*, *10*(1), 83–89. https://doi.org/10.1175/1520-0485(1980)010<0083:eotlro>2.0.co;2

Padman, L., & Dillon, T. M. (1987). Vertical heat fluxes through the Beaufort Sea thermohaline staircase. *Journal of Geophysical Research*, *92*(C10), 10799–10806. https://doi.org/10.1029/jc092ic10p10799

Palmer, M. R., Stephenson, G. R., Inall, M. E., Balfour, C., Düsterhus, A., & Green, J. A. M. (2015). Turbulence and mixing by internal waves in the Celtic Sea determined from ocean glider microstructure measurements. *Journal of Marine Systems*, *144*, 57–69. https://doi.org/10.1016/j.jmarsys.2014.11.005

Peterson, A. K., & Fer, I. (2014). Dissipation measurements using temperature microstructure from an underwater glider. *Methods in Oceanography*, *10*, 44–69. https://doi.org/10.1016/j.mio.2014.05.002

Plueddemann, A. J., & Farrar, J. T. (2006). Observations and models of the energy flux from the wind to mixed-layer inertial currents. *Deep Sea Research Part II: Topical Studies in Oceanography*, *53*(1), 5–30. https://doi.org/10.1016/j.dsr2.2005.10.017

Pollard, R. T., & Millard, R. C. (1970). Comparison between observed and simulated wind-generated inertial oscillations. *Deep Sea Research and Oceanographic Abstracts*, *17*(4), 813–821. https://doi.org/10.1016/0011-7471(70)90043-4

Polzin, K. L., Toole, J. M., Ledwell, J. R., & Schmitt, R. W. (1997). Spatial variability of turbulent mixing in the abyssal ocean. *Science*, *276*(5309), 93–96. https://doi.org/10.1126/science.276.5309.93

Rignot, E., Jacobs, S., Mouginot, J., & Scheuchl, B. (2013). Ice-shelf melting around Antarctica. *Science*, *341*(6143), 266–270. https://doi.org/10.1126/science.1235798

Robertson, R., Padman, L., & Levine, M. D. (1995). Fine structure, microstructure, and vertical mixing processes in the upper ocean in the western Weddell Sea. *Journal of Geophysical Research*, *100*(C9), 18517–18535. https://doi.org/10.1029/95jc01742

Rott, H., Rack, W., Skvarca, P., & Angelis, H. D. (2002). Northern Larsen Ice Shelf, Antarctica: Further retreat after collapse. *Annals of Glaciology*, *34*, 277–282. https://doi.org/10.3189/172756402781817716

Ruddick, B. (1983). A practical indicator of the stability of the water column to double-diffusive activity. *Deep Sea Research Part A. Oceanographic Research Papers*, *30*(10), 1105–1107. https://doi.org/10.1016/0198-0149(83)90063-8

Schultze, L. K. P., Merckelbach, L. M., & Carpenter, J. R. (2017). Turbulence and mixing in a shallow shelf sea from underwater gliders. *Journal of Geophysical Research: Oceans*, *122*(11), 9092–9109. https://doi.org/10.1002/2017jc012872

Stammerjohn, S. E., Martinson, D. G., Smith, R. C., & Iannuzzi, R. A. (2008). Sea ice in the western Antarctic Peninsula region: Spatio-temporal variability from ecological and climate change perspectives. *Deep Sea Research Part II: Topical Studies in Oceanography*, *55*(18–19), 2041–2058. https://doi.org/10.1016/j.dsr2.2008.04.026

Stigebrandt, A. (1999). Resistance to barotropic tidal flow in straits by baroclinic wave drag. *Journal of Physical Oceanography*, *29*(2), 191–197. https://doi.org/10.1175/1520-0485(1999)029<0191:rtbtfi>2.0.co;2

Thomas, L. N., & Lee, C. M. (2005). Intensification of ocean fronts by down-front winds. *Journal of Physical Oceanography*, *35*(6), 1086–1102. https://doi.org/10.1175/jpo2737.1

Trenberth, K. E., Large, W. G., & Olson, J. G. (1990). The mean annual cycle in global ocean wind stress. *Journal of Physical Oceanography*, *20*(11), 1742–1760. https://doi.org/10.1175/1520-0485(1990)020⟨1742:TMACIG⟩2.0.CO;2

Turner, J., Maksym, T., Phillips, T., Marshall, G. J., & Meredith, M. P. (2013). The impact of changes in sea ice advance on the large winter warming on the western Antarctic Peninsula. *International Journal of Climatology*, *33*(4), 852–861. https://doi.org/10.1002/joc.3474

Venables, H. J., Clarke, A., & Meredith, M. P. (2013). Wintertime controls on summer stratification and productivity at the western Antarctic Peninsula. *Limnology & Oceanography*, *58*(3), 1035–1047. https://doi.org/10.4319/lo.2013.58.3.1035

Venables, H. J., & Meredith, M. P. (2014). Feedbacks between ice cover, ocean stratification, and heat content in Ryder Bay, western Antarctic Peninsula. *Journal of Geophysical Research: Oceans*, *119*(8), 5323–5336. https://doi.org/10.1002/2013jc009669

Venables, H. J., Meredith, M. P., & Brearley, J. A. (2017). Modification of deep waters in Marguerite Bay, western Antarctic Peninsula, caused by topographic overflows. *Deep Sea Research Part II: Topical Studies in Oceanography*, *139*, 9–17. https://doi.org/10.1016/j.dsr2.2016.09.005

Wallace, M. I., Meredith, M. P., Brandon, M. A., Sherwin, T. J., Dale, A., & Clarke, A. (2008). On the characteristics of internal tides and coastal upwelling behavior in Marguerite Bay, west Antarctic Peninsula. *Deep Sea Research Part II: Topical Studies in Oceanography*, *55*(18–19), 2023–2040. https://doi.org/10.1016/j.dsr2.2008.04.033

Wolk, F., Yamazaki, H., Seuront, L., & Lueck, R. G. (2002). A new free-fall profiler for measuring biophysical microstructure. *The Journal of Atmospheric and Oceanic Technology*, *19*(5), 780–793. https://doi.org/10.1175/1520-0426(2002)019<0780:anffpf>2.0.co;2

Wunsch, C., & Ferrari, R. (2004). Vertical mixing, energy, and the general circulation of the oceans. *Annual Review of Fluid Mechanics*, *36*(1), 281–314. https://doi.org/10.1146/annurev.fluid.36.050802.122121